

Article

Self-Adaptive High-Frequency Injection Based Sensorless Control for Interior Permanent Magnet Synchronous Motor Drives [†]

Piyush Kumar ¹, Omar Bottesi ¹, Sandro Calligaro ^{1,*}, Luigi Alberti ²  and Roberto Petrella ³

¹ Faculty of Science and Technology, Free University of Bozen-Bolzano, 39100 Bolzano, Italy; piyush.kumar@natec.unibz.it (P.K.); omar.bottesi@unibz.it (O.B.)

² Department of Industrial Engineering, University of Padova, 35122 Padova, Italy; luigi.alberti@unipd.it

³ Polytechnic Department of Engineering and Architecture, University of Udine, 33100 Udine, Italy; roberto.petrella@uniud.it

* Correspondence: sandro.calligaro@unibz.it

[†] This paper is an extended version of the paper “Self-adaptive high-frequency injection based sensorless control for IPMSM and SynRM” presented to SLED 2017 Conference, 18–19 September, Catania, Italy, and published in 2017 IEEE International Symposium on Sensorless Control for Electrical Drives (SLED).

Received: 26 August 2019; Accepted: 18 September 2019; Published: 24 September 2019



Abstract: An auto-tuning and self-adaptation procedure for High Frequency Injection (HFI) based position and speed estimation algorithms in Interior Permanent Magnet Synchronous Motor (IPMSM) drives is proposed in this paper. Analytical developments show that, using conventional approaches, the dynamics of the high-frequency tracking loop varies with differential inductances, which in turn depend on the machine operating point. On-line estimation and adaptation of the small signal gain of the loop is proposed here, allowing accurate auto-tuning of the sensorless control scheme which does not rely on a priori knowledge of the machine parameters. On-line adaptation of Phase-Locked Loop (PLL) gains and of the injected voltage magnitude is also possible, leading to important advantages from the performance, loss and acoustic point of view. The theoretical basis of the method has been introduced first and the main concept demonstrated by means of simulations. Implementation has been carried out using the hardware of a commercial industrial drive and two Interior Permanent Magnet Synchronous Motors, namely a prototype and an off-the-shelf machine. Experimental tests demonstrate the feasibility and effectiveness of the proposal.

Keywords: IPMSM drives; adaptive control; high frequency injection; sensorless

1. Introduction

Due to the increasing demand for efficiency, drives based on Permanent Magnet Synchronous Machines (PMSM) and Synchronous Reluctance Machines (SynRM) are foreseen to become more and more popular. Since their control requires position and speed information, sensorless control is often adopted due to cost and reliability reasons. With sensorless control, complexity increases due to a larger number of control parameters and manual tuning (which is generally performed by trained technicians) becomes tedious and difficult. Moreover, the possibility to run several tests might be restricted, e.g., for safety or mechanical constraints, especially in industrial applications. Wide adoption of these drives poses even greater obstacles due to dependence on prior information about machine parameters, which in turn may depend on the operating point. Self-commissioning procedures for identification, [1–4], and tuning of all the control parameters, including those related to the sensorless estimation, are highly desirable. The self-commissioning procedure itself might require the use of

position estimation, e.g., in [5] a High Frequency Injection (HFI) method is used for rotor position estimation during flux vs. current maps identification at stand still.

The main HFI based methods proposed in literature for rotor position estimation are the INFORM method [6], rotating [7,8], and pulsating [9,10] injection based, square-wave injection based [11], arbitrary injection based [12], and PWM excitation based [13,14]. In most cases, HFI based position and speed estimation algorithms for IPMSM and SynRM drives are implemented by means of a feedback approach, based on a Phase Locked Loop (PLL) scheme, [7–13]. The estimated position is virtually compared to the real position in order to yield a correction term. This is usually obtained in the form of an error signal, which is normally proportional to the sine of twice the position error. This signal is then fed to a PI regulator, which drives the PLL or a mechanical model of the system. If the small-signal approach is considered, the amplitude of the error correction signal corresponds to a gain within the equivalent dynamics of the PLL and ultimately affects the performances and stability properties of position and speed estimation. Unfortunately, this parameter depends on differential inductances [15], which can vary with the machine operating point due to magnetic saturation, especially in IPMSM and SynRM. In fact, while cross-saturation causes steady-state estimation error [15–18] and is closely related to the high-frequency estimation model, self-saturation changes the equivalent estimation loop transfer function and should be taken into account to guarantee a proper response of the tracking loop in every magnetic operating condition of the machine. Independent of the specific PLL or mechanical observer design procedure adopted (e.g., [19,20]), obtaining stable and repeatable estimation dynamics is highly desirable. Speed adaptive observer has been proposed in [21], where observer gains design is proposed by linearizing the motor model and observer. This gain results in increased damping and higher noise suppression. Various methods and approaches have been proposed in the literature for identification of HF frequency and fundamental effects during transients, a model-based controller design has been proposed in [16,22] where two-degree of freedom in control has been used to separate the fundamental and HF effects during transient stages. A modified feed-forward control has been demonstrated for mid- to high-speed range operations, eliminating the need of any additional back EMF estimator. A single voltage vector injection-based method has been presented in [23] which is linked to the term containing position error without need of any additional filters, also with low computational burden.

Considering the state-of-the-art represented in literature, although many issues related to the HF injection algorithms have been addressed, the tuning of the parameters of HF injection-based estimation algorithms (which are mainly represented by filter bandwidth values and gains) remains problematic. In [19,20], the design is reported, based on the motor parameters, namely the HF inductances or small-signal (“differential”) inductances. In many cases (e.g., in the case of general-purpose industrial drives, which is one of the target applications of this paper), these parameters are usually not known in detail. Moreover, as already mentioned, they could be identified with insufficient accuracy and be variable because of magnetic saturation effects. As a result, properly setting the estimation algorithm gains becomes a difficult operation, which practically may require manual tuning.

The work presented in this paper aims at overcoming the problems related to dynamics in the presence of uncertain, unknown or varying small-signal gain of the estimation algorithm. With the adoption of the proposed method, the dynamical behavior of the position and speed tracking becomes independent of the motor parameters. The additional introduction of a method for regulating the “strength” of the useful HF signal (i.e., the amplitude of HF anisotropy-related current) allows to apply a proper voltage injection, which may be optimized in terms of robustness or in order to minimize losses, acoustic noise and vibrations. In order to obtain these results, on-line estimation and adaptation of the gains of the PLL, presented for the first time in [24], is applied, so that the design of the estimation loop gains and filters can be performed without any prior knowledge about the motor differential inductances. A certain set of PLL parameters, in fact, achieves approximately the same dynamical performance in position and speed estimation on any motor (provided that it exhibits sufficient anisotropy) and under different operating conditions. Furthermore, the proposed method

gives the possibility to adapt the high frequency injection voltage amplitude, in order to achieve a constant high frequency current excitation, i.e., a certain amplitude of the useful test signal. The same kind of objective has been pursued for square wave HFI in a recent research paper [25].

The effectiveness of the technique has been tested in simulation and on a real-world implementation platform (i.e., the hardware of a commercial inverter) using two different machines, demonstrating its potential for immediate deployment. The analytical developments and the self-adaptation method have been preliminarily tested by considering the step response of the estimation PLL, with very good agreement between theoretical and experimental results, demonstrating that estimation dynamics can be made independent of operating conditions and injection voltage magnitude. Further testing comprises sensorless control, especially in comparison to the traditional method (without adaptation). The method represents an important leap towards the self-commissioning and automatic tuning of high-frequency injection based sensorless IPMSM drives.

2. Rotating-Voltage High-Frequency Injection: State-Of-The-Art

The electric model of an Interior Permanent Magnet machine can be written in the synchronous reference frame, using the Park notation [26]:

$$v_{dq} = R_s i_{dq} + \frac{d}{dt} \lambda_{dq} + \begin{bmatrix} 0 & -1 \\ 1 & 0 \end{bmatrix} \omega_{me} \lambda_{dq} \quad (1)$$

where v_{dq} correspond to phase voltage, i_{dq} denotes current, ω_{me} is the mechanical-electrical speed, R_s is the phase resistance and λ_{dq} indicates flux-linkage.

Signal injection for sensorless control purposes is applied at much higher frequency than the fundamental (e.g., hundreds or thousands of Hz vs. tens or hundreds of Hz), especially considering that the HFI methods are meant for low-speed operation. If the analysis is restricted to the high-frequency behavior, the resistive voltage drop can be neglected [7,9] since phase resistance is much smaller than inductive reactance. This condition holds in most cases also for low-power machines, having large resistance, such as those considered in this paper (worst-case is for motor #1, where d -axis inductive reactance is more than 40 times larger than phase resistance). The fundamental motional voltage, i.e., the terms proportional to mechanical-electrical speed ω_{me} , can be disregarded, since it belongs, by definition, to the fundamental frequency. Equation (1) can be approximated as

$$v_{i,dq} \approx \frac{d}{dt} \lambda_{i,dq} \quad (2)$$

In (2) and in the following, subscript i will be used for injection-related variables, i.e., the voltage corresponding to the high-frequency injected signal and the consequent current and flux-linkage components. The small-signal approximation will be applied, in order to deal with the analytical issues related to non-linearity.

In the HF injection method adopted here, based on [7], a high-frequency voltage vector $v_{i,\alpha\beta}$, rotating at ω_i angular frequency with amplitude V_i , is superimposed to the fundamental voltage needed for torque control:

$$v_{i,\alpha\beta} = V_i \begin{bmatrix} -\sin \omega_i t \\ \cos \omega_i t \end{bmatrix} \quad (3)$$

The consequent high-frequency flux-linkage components can be calculated both in the stationary and in the synchronous reference frames:

$$\lambda_{i,\alpha\beta} = \frac{V_i}{\omega_i} \begin{bmatrix} \cos \omega_i t \\ \sin \omega_i t \end{bmatrix} \quad (4)$$

$$\lambda_{i,dq} = \frac{V_i}{\omega_i} \begin{bmatrix} \cos(\omega_i t - \theta_{me}) \\ \sin(\omega_i t - \theta_{me}) \end{bmatrix} \quad (5)$$

the (local) differential inductances

$$l_d \triangleq \frac{d\lambda_d}{di_d}, \quad l_q \triangleq \frac{d\lambda_q}{di_q} \quad (6)$$

can be defined, so for small-signal operation the flux-linkage vector can also be expressed as a function of current (cross-saturation effects are neglected in these calculations):

$$\lambda_{i,dq} = \begin{bmatrix} l_d & 0 \\ 0 & l_q \end{bmatrix} \mathbf{i}_{i,dq} \quad (7)$$

The last equation can be used for obtaining the high-frequency currents, by dividing the d - and q -axis flux-linkage by small-signal inductances. This results in the current vector

$$\mathbf{i}_{i,dq} = \frac{V_i}{\omega_i} \begin{bmatrix} 1/l_d \cos(\omega_i t - \theta_{me}) \\ 1/l_q \sin(\omega_i t - \theta_{me}) \end{bmatrix} \quad (8)$$

Equation (8) can be rewritten as

$$\begin{aligned} \mathbf{i}_{i,dq} &= \frac{V_i}{\omega_i(l_\Sigma^2 - l_\Delta^2)} \left(l_\Sigma \begin{bmatrix} \cos(\omega_i t - \theta_{me}) \\ \sin(\omega_i t - \theta_{me}) \end{bmatrix} + l_\Delta \begin{bmatrix} \cos(-\omega_i t + \theta_{me}) \\ \sin(-\omega_i t + \theta_{me}) \end{bmatrix} \right) \\ &= i_{i0} \begin{bmatrix} \cos(\omega_i t - \theta_{me}) \\ \sin(\omega_i t - \theta_{me}) \end{bmatrix} + i_{i1} \begin{bmatrix} \cos(-\omega_i t + \theta_{me}) \\ \sin(-\omega_i t + \theta_{me}) \end{bmatrix} \end{aligned} \quad (9)$$

by using definitions of average (“ Σ ” subscript) and half-difference (“ Δ ” subscript) inductances:

$$l_\Sigma \triangleq \frac{l_q + l_d}{2}, \quad l_\Delta \triangleq \frac{l_q - l_d}{2} \quad (10)$$

and additional definitions of two current magnitude values

$$i_{i0} \triangleq \frac{V_i l_\Sigma}{\omega_i(l_\Sigma^2 - l_\Delta^2)}, \quad i_{i1} \triangleq \frac{V_i l_\Delta}{\omega_i(l_\Sigma^2 - l_\Delta^2)} \quad (11)$$

It is straightforward to notice that the amplitude of the high-frequency current depends on the injection voltage magnitude V_i , on signal frequency ω_i and on the differential inductances, i.e., it is also a function of the magnetic operating condition of the machine.

Transforming back to the stationary reference frame, one obtains:

$$\mathbf{i}_{i,\alpha\beta} = i_{i0} \begin{bmatrix} \cos(\omega_i t) \\ \sin(\omega_i t) \end{bmatrix} + i_{i1} \begin{bmatrix} \cos(2\theta_{me} - \omega_i t) \\ \sin(2\theta_{me} - \omega_i t) \end{bmatrix} \quad (12)$$

According to the original method [7], demodulation is performed applying rotation by $-2\hat{\theta}_{me} + \omega_i t$, where $\hat{\theta}_{me}$ is the position estimate. This results in the vector signal $\mathbf{i}_{i,demod}$, containing the two orthogonal projections $i_{i,demod_x}$ and $i_{i,demod_y}$ on x and y axes, respectively:

$$\begin{aligned} \mathbf{i}_{i,demod} &= \begin{bmatrix} i_{i,demod_x} \\ i_{i,demod_y} \end{bmatrix} = \begin{bmatrix} \cos(-2\hat{\theta}_{me} + \omega_i t) & \sin(-2\hat{\theta}_{me} + \omega_i t) \\ -\sin(-2\hat{\theta}_{me} + \omega_i t) & \cos(-2\hat{\theta}_{me} + \omega_i t) \end{bmatrix} \mathbf{i}_{i,\alpha\beta} \\ &= i_{i0} \begin{bmatrix} \cos(2\omega_i t - 2\hat{\theta}_{me}) \\ \sin(2\omega_i t - 2\hat{\theta}_{me}) \end{bmatrix} + i_{i1} \begin{bmatrix} \cos(2\theta_{me} - 2\hat{\theta}_{me}) \\ \sin(2\theta_{me} - 2\hat{\theta}_{me}) \end{bmatrix} \end{aligned} \quad (13)$$

The low-frequency content of $i_{i,demod}$ is then extracted by means of a Low-Pass Filter (LPF), i.e.,

$$LPF\{i_{i,demod}\} = LPF\left\{\begin{bmatrix} i_{i,demod_x} \\ i_{i,demod_y} \end{bmatrix}\right\} = i_{i1} \begin{bmatrix} \cos(2\theta_{me} - 2\hat{\theta}_{me}) \\ \sin(2\theta_{me} - 2\hat{\theta}_{me}) \end{bmatrix} \quad (14)$$

A signal for correction e can be obtained by selecting the second-row component of (14), i.e.,

$$e = \begin{bmatrix} 0 & 1 \end{bmatrix} \cdot LPF\{i_{i,demod}\} = LPF\{i_{i,demod_y}\} = LPF\{i_{i1} \cdot \sin[2(\theta_{me} - \hat{\theta}_{me})]\} \quad (15)$$

A block diagram representing the position estimation algorithm based on rotating voltage HFI [7] is shown in Figure 1, where $R(\theta)$ represents the vector transformation as per Equation (13). The first signal out of the transformation block, $i_{i,demod_x}$, is discarded, while the second, $i_{i,demod_y}$, is exploited as the error correction signal, after proper filtering.

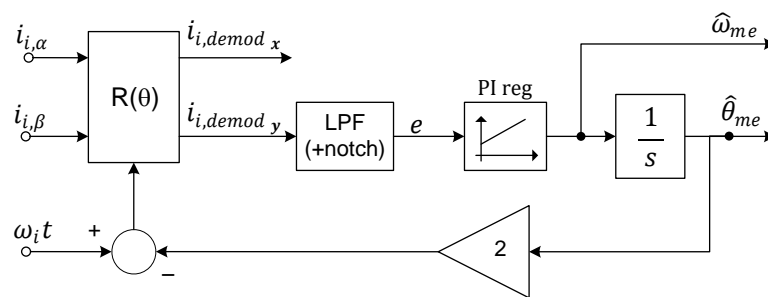


Figure 1. Typical algorithm for position estimation based on rotating-voltage High Frequency Injection (HFI) [7].

3. Estimation PLL Dynamics and Tuning

With respect to other methods (e.g., fundamental-based), the dynamics of HFI-based speed and position estimation has been investigated less extensively. However, effective analytical approaches for PLL gains design have been proposed, e.g., [19,20], where the specific aspects of these methods, such as the effect of filtering and demodulation, are taken into account. In fact, as mentioned in the introduction, manual tuning might be restricted or even unacceptable in certain cases, due to many reasons. On the other hand, analytical tuning strongly relies on the knowledge of differential inductances, which are often unavailable for off-the-shelf machines and usually vary with the operating point, due to magnetic saturation.

The proposed analysis of dynamics is similar in principle to the one in [20], where linearization is applied and the frequency response of filters is considered in order to obtain a straightforward representation of the loop dynamics, which represents the basis of the proposed method.

Considering small values of the error, the non-linear sine function can be approximated to its argument, i.e., from the dynamics point of view the small-signal equivalent of the error signal will be

$$e \approx LPF\{2 i_{i1} \cdot (\theta_{me} - \hat{\theta}_{me})\} \quad (16)$$

The error signal is approximately proportional to the difference between actual and estimated position, with a gain $2i_{i1}$, followed by a low-pass filter, which represent the physical effect of the inductive behavior of motor phases and the dynamics of the demodulation process. The obtained signal is fed to a PI controller, followed by an integrator, in order to obtain the position signal from the speed estimate. The position estimate is then used for the calculation of vector rotation in the first part of (13). The equivalent block diagram, which can be conveniently adopted for loop dynamics analysis and PLL regulator design, is shown in Figure 2.

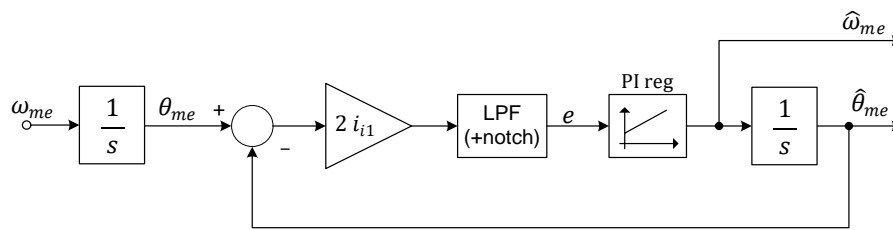


Figure 2. Equivalent block diagram of the position estimation algorithm considered for dynamics design of the loop shown in Figure 1.

Considering the definition of i_{i1} (11), Equation (16) shows that the equivalent gain of the error signal depends on differential inductances. These vary due to magnetic saturation, which means that insufficient estimation bandwidth or, on the other hand, instability can occur if constant gains are considered in the tracking loop. In general, these effects make it difficult to obtain optimal performance in the entire range of operation with constant tracking gains. To showcase the effect of saturation, the flux-linkage maps of one of the IPM machine considered in the following simulations and experiments are reported in Figure 3.

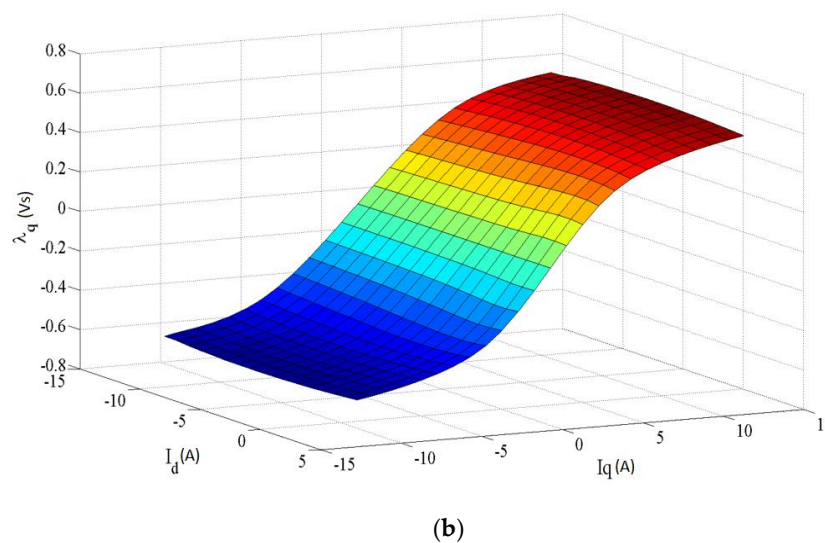
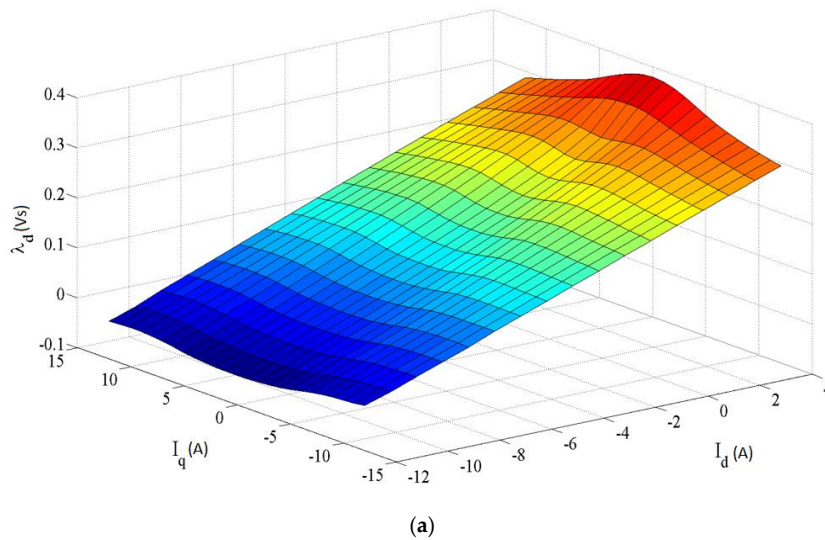


Figure 3. Flux-linkage maps of motor #1 for the d -axis (a) and q -axis (b).

If the value of i_{i1} is known, e.g., thanks to characterization measurements, it can be taken into account, allowing to design the regulator aiming at a certain goal, e.g., in terms of bandwidth and stability margins. To attain this, an effective approach is to approximate the objective estimation bandwidth $\omega_{HF_{BW}}$ with the cross-over frequency of the open-loop transfer function. Based on the PLL schematic in Figure 2, the transfer function can be easily obtained:

$$G_{PLL_{OL}}(s) = 2 i_{i1} \left(K_{P_{PLL}} \frac{1 + \tau_{PLL} s}{\tau_{PLL} s} \right) \frac{1}{s} LPF(s) \quad (17)$$

where $K_{P_{PLL}}$ is the PI gain and τ_{PLL} is the PI regulator time constant, i.e., the ratio between proportional and integral gains, while $LPF(s)$ is the filter transfer function. In order to ensure stability (i.e., about -20 dB/dec slope at 0 dB gain in the Bode diagram), the closed-loop bandwidth must be comprised between the PI zero and the LPF bandwidth ω_{LPF} , i.e., $\frac{1}{\tau_{PLL}} < \omega_{HF_{BW}} < \omega_{LPF}$. Practically, $\omega_{HF_{BW}}$ must be sufficiently distant from these extremes, i.e., at least double the bottom limit and half the top limit. If this condition is satisfied, the transition frequency is approximately

$$\omega_{HF_{BW}} = 2i_{i1} K_{P_{PLL}} \quad (18)$$

This equation allows to set the proportional gain, once the value of i_{i1} is known and constant. In the following simulation and experiments, the cross-over frequency is chosen to be 2.5 times lower than the LPF bandwidth and 3 times larger than the PI pole frequency. A notch filter centered on the injection frequency is added in order to reject the effect of fundamental, finally resulting in the transfer functions shown in Figure 4. In general, optimal choices in the design of the gains also involve considerations on the overall control dynamics (e.g., desired speed control bandwidth vs. noise and ripple), which are out of the scope of this paper.

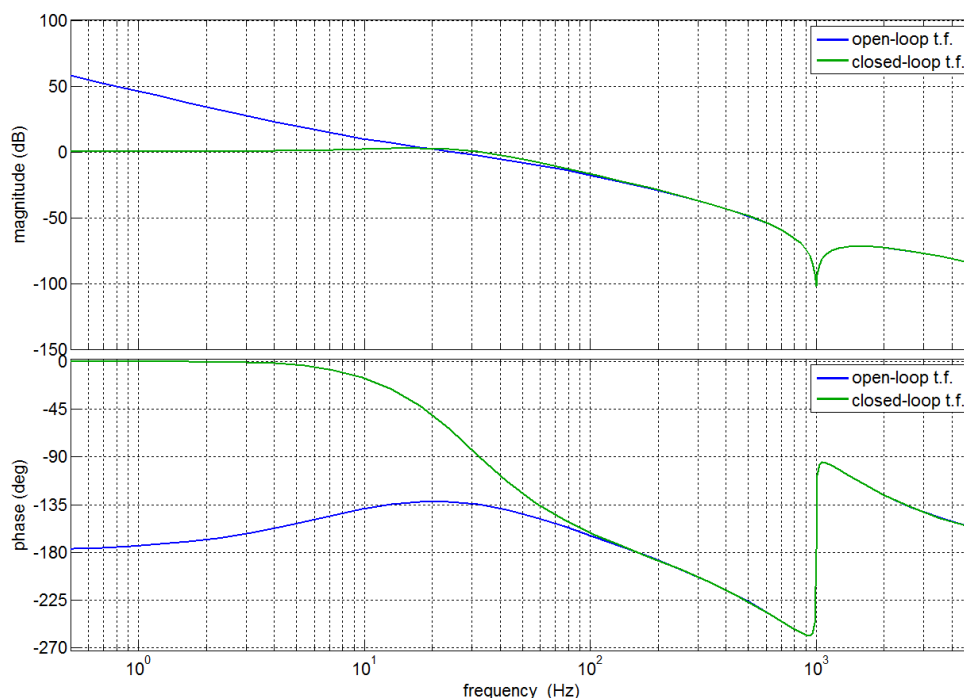


Figure 4. Bode diagram of the open-loop and closed-loop transfer functions representing the dynamics of the Phase-Locked Loop (PLL) schematic in Figure 2.

4. Proposed Self-Adaptive Method and Auto-Tuning of Sensorless Control

In the proposed method for PLL gains adaptation, the equivalent gain factor i_{i1} is estimated on-line and compensated for. As a result, the design of the estimation dynamics is made independent

of the motor differential inductances, then a certain set of PLL gains results in approximately the same response under different motors and conditions. Cross-saturation (i.e., the presence of non-zero mutual small-signal inductances), will be neglected in the following analysis, in order to simplify analytical calculation and highlight the main aspects of the proposed self-adaptive method. In fact, cross-saturation affects the accuracy of the overall sensorless control (introducing a steady-state position estimation error), as reported in [15–18], but is expected to have negligible contribution on the dynamics (which has been confirmed by experiments). Possible effects of mutual inductance on estimation dynamics will be the topic of future investigation.

In the considered rotating-voltage injection approach (as opposed to the pulsating one, [8]), two signals proportional to the sine and cosine of the error can be obtained, as shown in (14), although only the sine signal is usually exploited in literature. Obtaining the complete error vector (14) means that an estimate of the amplitude of the error correction signal i_{i1} can be calculated as the norm of the vector:

$$\hat{i}_{i1} = \|\text{LPF}\{i_{demod}\}\| = \|\text{LPF}\left\{\begin{bmatrix} i_{i,demod_x} \\ i_{i,demod_y} \end{bmatrix}\right\}\| \approx \text{LPF}\left\{i_{i1} \begin{bmatrix} \cos(2\theta_{me} - 2\hat{\theta}_{me}) \\ \sin(2\theta_{me} - 2\hat{\theta}_{me}) \end{bmatrix}\right\} = \text{LPF}\{i_{i1} \cdot 1\} \quad (19)$$

Since the norm of the sine-cosine vector is unity, this processing leads to an estimate the error signal magnitude value \hat{i}_{i1} . Finally, this allows to normalize the error signal, dividing it by twice the obtained value, i.e.:

$$\frac{e}{2\hat{i}_{i1}} = \frac{1}{2} \frac{e}{\|\text{LPF}\{i_{demod}\}\|} \approx \text{LPF}\{\theta_{me} - \hat{\theta}_{me}\} \quad (20)$$

From the Equation (20) it can be seen that, by applying this processing, the loop dynamics becomes independent of the HF current signal amplitude i_{i1} , i.e., it does not depend on inductances l_d, l_q , frequency and injected voltage magnitude V_i , contrary to the traditional method. In particular, given the desired dynamical behavior, the PLL regulator gains can be set constant for any operating condition and machine. The block diagram representing the proposed algorithm, including loop gain estimation and on-line adaptation feature, is shown in Figure 5, where the estimated value of i_{i1} is highlighted with a red box. The main difference with respect to the typical schematic (Figure 1) consists in the division of the error signal by twice the estimated HF current amplitude, which leads to gain normalization.

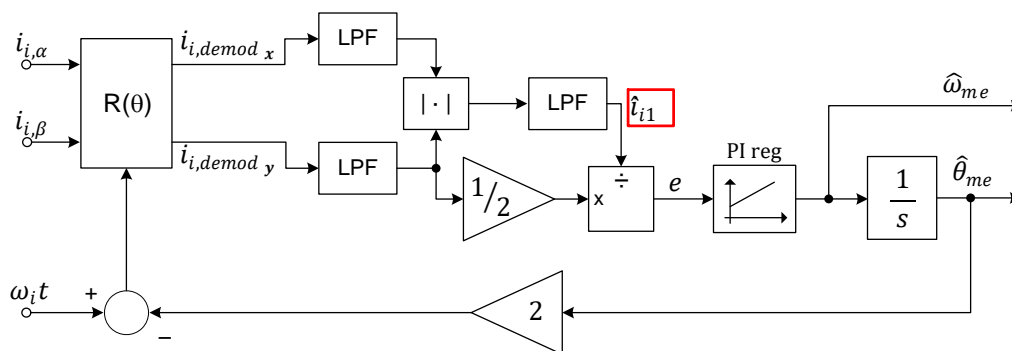


Figure 5. PLL schematic adopting the proposed gain adaptation.

The equivalent dynamics of the proposed algorithm can be represented by the schematic in Figure 2, except that the gain $2i_{i1}$ is substituted by unity gain. Making the dynamics independent of machine characteristics, operating point and injected signal amplitude is an important advantage, especially if auto-tuning of the control parameters needs to be provided. In fact, once the PLL gains and filters have been chosen and tested successfully for one case, the same settings are expected to give similar behavior in all other cases, comprising the application to different motors. The low-pass filtering on the i_{i1} estimation path should be designed so that the bandwidth is greater or equal to the speed regulation bandwidth. This may represent a limitation when very fast control dynamics is

desired, since wider bandwidth of \hat{i}_{i1} may lead to noisy estimate signal. In that case, normalization could be problematic (e.g., leading to artifacts), due to the non-linear division operation. These aspects will be the topic of future investigations.

In the experimental tests, as will be explained in Section 6, all the control algorithm has been implemented digitally on a microcontroller platform. The algorithm represented in Figure 5 can be split into basic algebraic operations on signals (e.g., gain, sum, division, and product) and filters such as low-pass, notch and integrator. These were implemented in software, after discretization. Coordinates transformation requires the use of trigonometric functions, for which a standard C math has been used.

5. Proposed Adaptation of the Injection Voltage Amplitude

Since small signal inductances vary, HF current amplitude changes with machine load, consequently affecting torque ripple and acoustic noise. Ideally, a certain current amplitude is ensured, so that signal-to-noise ratio is sufficiently high (i.e., robust estimation is possible) while at the same time vibrations are minimized. This can be also translated into requirements on i_{i1} and i_{i0} . While estimation of i_{i1} has been introduced above (see (19) and the red box in Figure 5), it is also possible to estimate the amplitude of the term related to average inductance l_{Σ} , i.e., i_{i0} .

An additional demodulation branch is implemented (not shown in Figure 5), i.e., applying a rotation by $-\omega_i t$,

$$\mathbf{i}_{demod}^{-\omega_i t} = \begin{bmatrix} \cos(-\omega_i t) & \sin(-\omega_i t) \\ -\sin(-\omega_i t) & \cos(-\omega_i t) \end{bmatrix} \mathbf{i}_{i,\alpha\beta} \quad (21)$$

isolating the first component of the vector and low-pass filtering will result in

$$LPF\{[1 \ 0] \cdot \mathbf{i}_{demod}^{-\omega_i t}\} \approx LPF\{i_{i0}\} \quad (22)$$

By means of the feedback loop shown in Figure 6 it is then possible to regulate the magnitude of the high-frequency anisotropy-related current i_{i1} , in order to keep it at the desired constant (and convenient) level. Since i_{i1} represents the HFI signal strength, it is in fact tightly related to signal-to-noise ratio of position and speed estimation. Depending on the measurements noise level, desired performances, and acceptable acoustic noise, a certain value will be set for i_{i1}^* . The choice of this value can be supposed to scale with the drive rated current (i.e., with its full-scale measurement value).

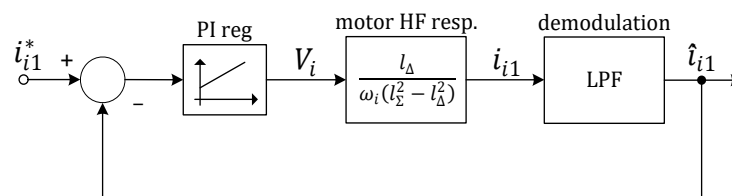


Figure 6. Regulation loop for anisotropy-related current magnitude: equivalent dynamics schematic.

The dynamics of the high-frequency current magnitude regulation loop can be approximated to a simple schematic, as shown in Figure 6. The low-pass filtering applied on the magnitude estimate signal introduces a dominant pole, which limits the possible regulation bandwidth. If an approximated value for differential inductances is available, it will suffice since tuning for a relatively slow control reaction is needed (e.g., having at least the same bandwidth as the speed regulation), and anyway the design is not required to obtain accurate dynamics (since voltage adaptation dynamics is not crucial). Given the simplicity of the equivalent dynamics, the only unknown block, i.e., the gain related to motor HF response (Figure 6) could be approximately estimated at the startup, imposing constant HF voltage and measuring the ratio i_{i1}/V_i . This could represent a viable solution to the issue of unknown inductances.

Similar to Figure 6, the magnitude of injection voltage signal can be adapted in a closed-loop fashion, aimed to obtaining a constant and known average high-frequency current magnitude i_{i0} (as

obtained in (22)), which is related to the torque ripple and acoustic noise. The anisotropy-related component can be regulated in order to achieve constant desired HF current magnitude by adapting the injection voltage. Since it is obtained by means of a closed-loop regulation, proper tuning of the regulator is also required. This can be simply achieved by using even coarse values of inductances.

It is worth mentioning that, once both i_{i0} and i_{i1} have been estimated, it would be possible (*although not required* for implementing the proposal) to estimate differential inductances l_d and l_q (which may be useful, e.g., for adaptation of the current control gains), by simply using the definition of current magnitude values i_{i0}, i_{i1} (11) and inductances l_{Σ}, l_{Δ} (10):

$$\hat{l}_d = \frac{V_i}{\omega_i(\hat{i}_{i0} + \hat{i}_{i1})}, \quad \hat{l}_q = \frac{V_i}{\omega_i(\hat{i}_{i0} - \hat{i}_{i1})} \quad (23)$$

6. Simulation Results

A model of the full drive system for speed control was built for validating the proposal. In particular, the IPM motor #1 (Figure 7), whose parameters are reported in Table 1, has been considered for the initial testing and tuning of the controller. The machine model (implemented in continuous-time) comprises cross-saturation effects, according to the maps shown in Figure 3 (obtained from laboratory rotational tests). The correctness of analytical development, comprising the rules for PLL tuning, has been proved in simulation, demonstrating the speed control capabilities. Since the adoption of HFI techniques in general considers sensorless control at low-speed as the main target, tests have only been performed in that range. Normal compensation of the injection and processing delay (i.e., 1.5 times the sampling period) has been applied. Possible additional issues related to higher speed operation are out of the scope of this paper.

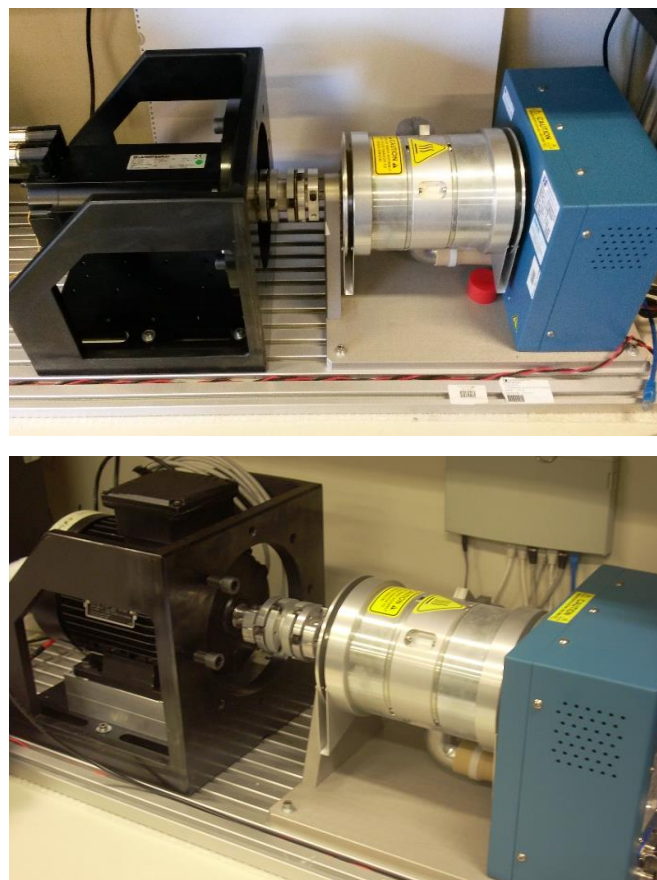
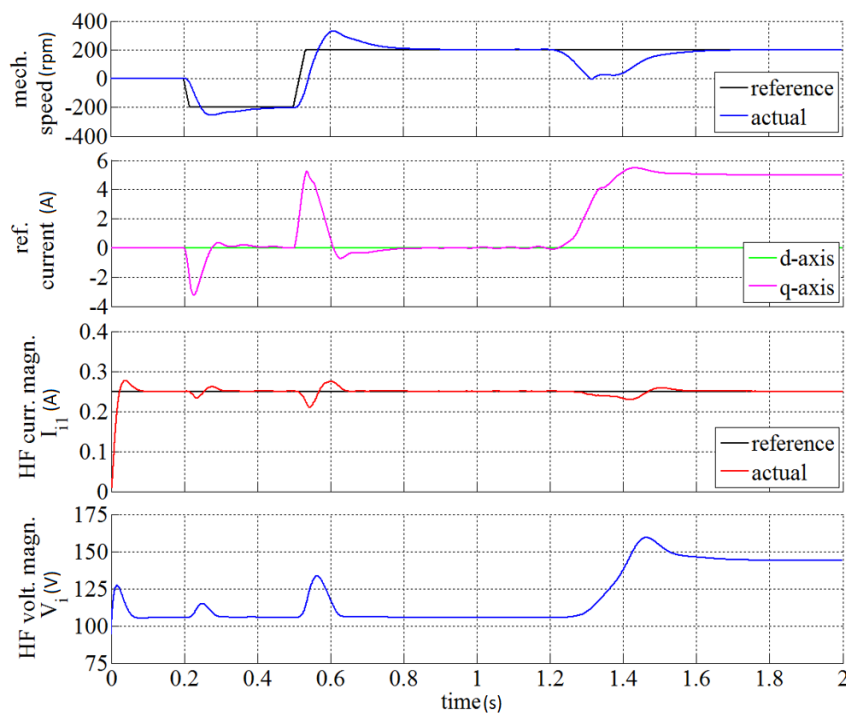


Figure 7. Test-bench used for the experimental investigations: motor #1 (top) and motor #2 (bottom) connected to the hysteresis brake.

Table 1. Rated Parameters of Interior Permanent Magnet (IPM) Machines.

	Motor #1	Motor #2	Units
Torque	6.7	7	Nm
Speed	3000	3000	rpm
Voltage (<i>phase-to-phase</i>)	330	290	V _{RMS}
Current	4.2	4.7	A _{RMS}
Pole pairs	2	5	-
Linearized <i>d</i> -/ <i>q</i> -axis inductance	22/95	12/17	mH
Resistance	3.4	1.2	Ω
Phase resistance	3.4	1.2	[Ω]
PM flux linkage	0.237	0.141	V s

An interesting simulation test, aimed at demonstrating the feasibility of the regulation of anisotropy-related signal amplitude i_{i1} , is reported in Figure 8. The schematic shown in Figure 6 has been implemented, applying reasonable limits to the regulator (in fact, injection voltage should be larger than the effect of dead-time and lower than the maximum available inverter voltage). As can be seen in Figure 8, the controlled current magnitude is kept close to the reference value of 0.25 A (third diagram from the top), while the drive performs different speed transients (from 0 to −200 rpm, from −200 to +200 rpm) and a load disturbance test at 200 rpm (0 to 50% rated load) in sensorless control. In order to make the effect of magnetic saturation more evident, null *d*-axis current has been applied in this case (instead of the MTPA trajectory), resulting in large *q*-axis current, which makes the motor enter a heavily saturated region (see Figure 3, *q*-axis). The loop automatically adapts the injection voltage magnitude, in order to obtain the desired signal strength. At high torque, the voltage needed for obtaining the desired high-frequency current magnitude is about 50% more than at no load. Full characterization of the estimation performances from this point of view (e.g., control stiffness and steady-state ripple vs. i_{i1} and/or i_{i0}) is out of the scope of this paper. However, experimental test results suggest that the best option is to operate at constant i_{i1} , since the same very small value $i_{i1} = 75$ mA guarantees very similar performances on both motors (i.e., withstanding rated torque disturbance).

**Figure 8.** Simulated High-Frequency (HF) anisotropy signal magnitude regulation during speed control start-up and transients (reference, load).

7. Experimental Results

The algorithm has been implemented in digital on the hardware of a commercial 5.5 kW drive (Gefran ADL 200), supplied by the three-phase grid (400 V_{RMS}). The control board is based on a microcontroller, equipped with floating-point unit and 12-bit Analog to Digital Converters (ADC). Suitable code development tools were made available by the manufacturer, within an industry–academia collaboration. Signal acquisition is carried out using a standard serial connection between the drive controller and a PC, after recording selected microcontroller variable samples on the embedded memory (maximum 4 variables and 8192 total samples per acquisition). The inverter switching frequency is 10 kHz, typical Space Vector Modulation with centered pulses and synchronous current sampling have been adopted. The use of a real-world industrial platform (i.e., no special or expensive devices are involved) demonstrates the potential for immediate deployment of the proposed technique.

Extensive investigation on dynamics and steady-state accuracy have been carried out on a 2.2 kW prototype IPMSM (main motor #1). In order to highlight the effectiveness of the proposed adaptation method and its independence of the motor characteristics, some tests have been repeated on a different one (Surface Mount-PMSM, motor #2), having almost the same power rating. Nominal motor parameters of both machines are reported in Table 1. The experimental setup comprises a hysteresis brake Magtrol HD-715 as the passive load, directly connected to the motor shaft, as already shown in Figure 7.

The first set of experiments has been devoted to demonstrating the effectiveness of the method, i.e., a pre-determined dynamics of the position estimation loop is maintained, despite any change in the actual i_{i1} current level. Corresponding test results are reported in Figure 9 (for motor #1) and Figure 10 (for motor #2). In both cases, the PLL response to a wrong initial estimated position at stand-still is shown. For a small initial position error (i.e., almost a linear behavior), this experiment corresponds to the typical small-signal step response test, applied to the estimation loop. The PLL is initially disabled (i.e., null PI gains), and a wrong (by approximately 0.25 rad) initial value is loaded onto the integrator term. Once the PLL is activated, the estimated position converges to the steady-state value (which ideally corresponds to the actual rotor position). In order to demonstrate the invariance of the PLL behavior (thanks to the automatic adaptation) despite any change in other parameters, the response at different values of injection voltage vector magnitude have been considered. No-load tests have been carried out for motor #1 (35, 70, and 140 V injection) and motor #2 (17, 35, 70, 140 V injection). Moreover, for motor #1, operation at different torque values (0, 3, and 6 Nm) has been also considered, while control used the MTPA strategy. In this case, load was applied by locking the rotor using the hysteresis passive brake. In order to ensure accurate and repeatable testing conditions (under load), the synchronous current control exploited the encoder position measurement, so that the operating point bias was not affected by position estimation error, while the HFI estimation algorithm was run in parallel. To the best of the authors' knowledge, this is the first time that the step response test of the HFI-based estimation PLL is reported and compared to the theoretical response, for many different conditions.

Although the topic of injected voltage minimization is out of the scope of this paper, it is worth to consider that, as will be shown in the next experimental tests, the minimum voltage required for robust speed control is not affected by the proposed method, i.e., the novel and the classical techniques require the same HF voltage. Moreover, based on technical information from reputable manufacturers of industrial inverters [27–29], injection voltage levels up to 25% of the available voltage are considered acceptable in industry (i.e., up to 80 V, in this case). Extending the survey with references from scientific literature [9,19,23,30–46], reveals that the injection level required for robust position estimation and sensorless control is widely variable, depending on many factors such as measurement noise, inverter and motor parameters, non-idealities and on the desired dynamics. For this reason, it is difficult to identify the minimum HF voltage which ensures robust sensorless operation, unless experiments on a specific system and application have been carried out. However, based on literature, a practically reasonable range for injection voltage amplitude can be considered from 5 to 20% of the DC-bus voltage

and 5 to 15% of the motor rated voltage. The HF voltage applied for sensorless control experiments in the next sections (i.e., from 30 to 60 V) is 6.4% to 12.8% of peak motor rated voltage and 5.4% to 10.9% of DC-bus voltage, i.e., in the low part of the range just mentioned. It should be noticed that 60 V are indeed only required when $i_d^* = 0$, while operation on the MTPA requires about 35 V for obtaining $I_{i1} = 75$ mA, almost independent of the load. The largest HF voltage value, i.e., 140 V, is applied in the tests of Figures 9 and 10 just for demonstration purposes, i.e., to showcase gain adaptation performance with respect to strongly varying conditions.

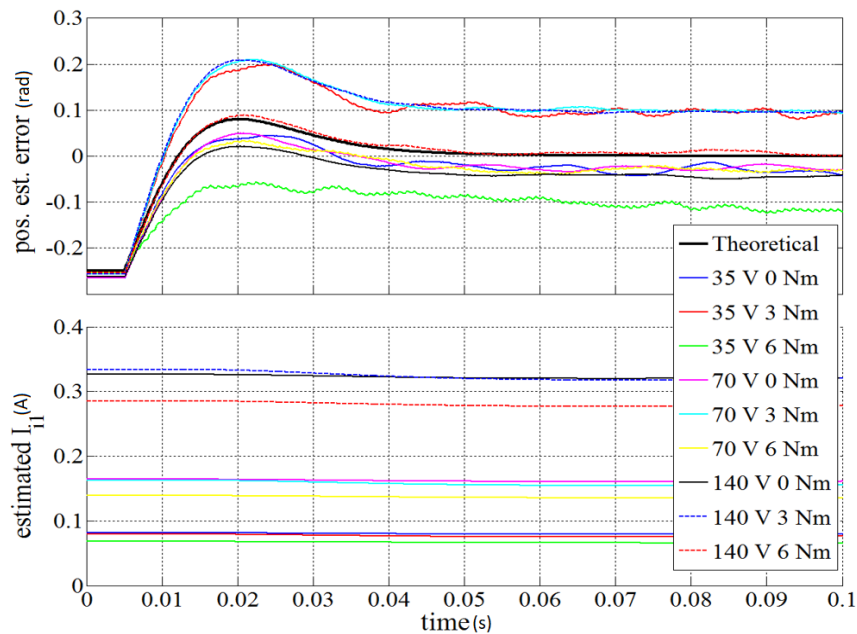


Figure 9. Step response of position tracking loop (motor #1).

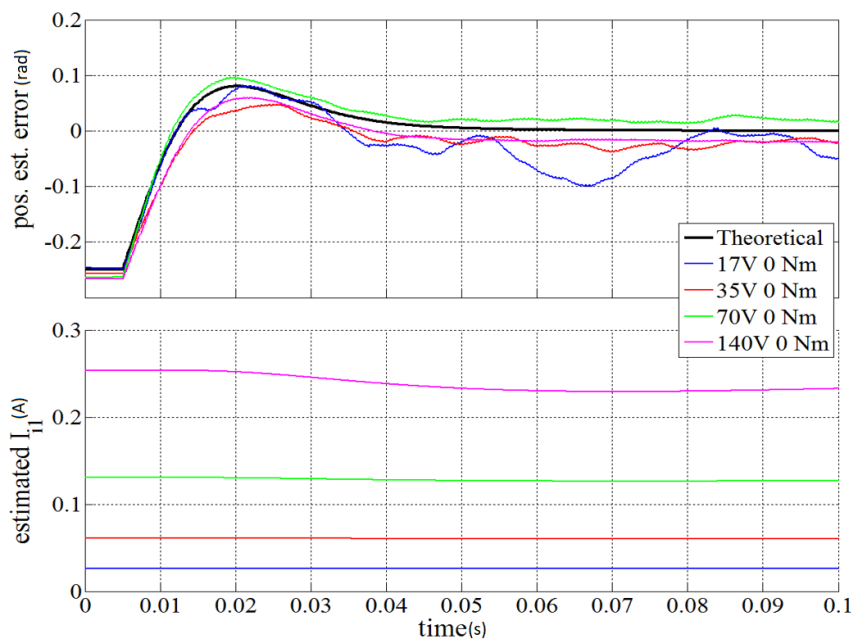


Figure 10. Step response of position tracking loop (motor #2).

It is also important to notice that HF injection methods are usually applied only at low-speed and stand-still. In fact, at medium- and high-speed fundamental wave-based methods can be successfully

adopted, which mostly exploit estimated back-EMF or flux-linkage [46–54]. Some of these techniques are based on fusion algorithms, i.e., information from both HF injection and fundamental quantities are exploited in the same PLL-like schematic [46–54]. Simpler proposals implement two different estimation methods and blend the resulting position and speed estimates at the PLL input [51–53] or output [54], where the HF injection is weighted more at low-speed and fundamental signals are trusted more at medium- to high-speed. The estimation method proposed in this paper can be easily integrated into a schematic of this kind. Injection can be disabled above a certain speed, avoiding unnecessary losses and additional acoustic noise. The full speed and torque range can then be reached, even if, at low-speed, a certain amount of voltage is reserved for HF injection. Fundamental-based and hybrid sensorless methods are out of the scope of this paper, which addresses specific aspects of signal injection based sensorless control.

Apart from the values of steady-state error (which are due to cross-saturation, as already pointed out), the different traces show very consistent dynamics, also compared to the theoretical (ideal) response (thick blue trace), despite the wide variations experienced by i_{i1} . The cases with 35 V injection, 6 Nm load in Figure 9 (motor #1) and 17 V injection, no-load in Figure 10 (motor #2) are exceptions, which can be explained considering that the large fundamental current, in combination with the inverter dead-time effect, causes large voltage distortion. In fact, since the DC-bus voltage is about 550 V, the lower injection level considered, 17 V, corresponds to approximately 3% of the bus voltage, while the dead-time accounts for 2.5% of the DC-bus voltage (interlock time is 2.5 μ s with respect to the 100 μ s PWM period), making this disturbance source almost dominant.

The position estimate is obtained from the phase of the selected HF current signal, which undergoes a relatively wide-bandwidth filtering before and through the PLL. On the other hand, the estimated i_{i1} represents the amplitude of the same HF current, which is more heavily low-pass filtered, resulting in almost flat behavior (bottom diagram). This explains the difference in the noise level, between the two traces.

The LPF and PI regulator tuning within the PLL have been chosen for approximately 25 Hz estimation bandwidth. This value allows to achieve satisfactory speed control performance, as requested by the tests reported in this paper, even though, in general, its value should be selected as a function of the application requirements. However, it can be surely stated that obtaining repeatable estimation dynamical response, independent of the adopted machine and operating point, allows to apply a certain tuning choice without any a priori knowledge of the machine parameters, which is an important step towards auto-tuning of the estimation algorithm.

Sensorless speed control has been first implemented and tested on motor #1, for the sake of validating the proposed technique and its effectiveness in different conditions, also comparing the novel method with classical (non-adapting) schemes. It is worth mentioning that, with respect to many real-world applications, the comprehensive inertia at the motor shaft is relatively small in this case, i.e., about three times the moment of inertia of the motor only. Given the current (and hence torque) limits and estimation noise level, the low-inertia condition is critical for sensorless control, due to the relatively large high acceleration possible and the low damping of speed ripple.

During all tests reported in figures from Figures 11–14, the injected voltage vector magnitude was 70 V and the speed regulation bandwidth was set to about 7 Hz. The MTPA trajectory was applied for current references generation from the torque reference (speed controller output). In the non-adapted case, the PLL gains were chosen considering the no-load value of i_{i1} obtained experimentally, while in the self-adapted algorithm this commissioning step was obviously not necessary. For each kind of test, the proposed method (self-adapted) is compared to the typical one (no adaptation).

No-load speed inversion tests have been reported in Figures 11 and 12. Reference speed is changed in a ramp between the initial value (–200 rpm) to the final value (+200 rpm). The actual speed is reversed in less than 100 ms and settles after about 200 ms.

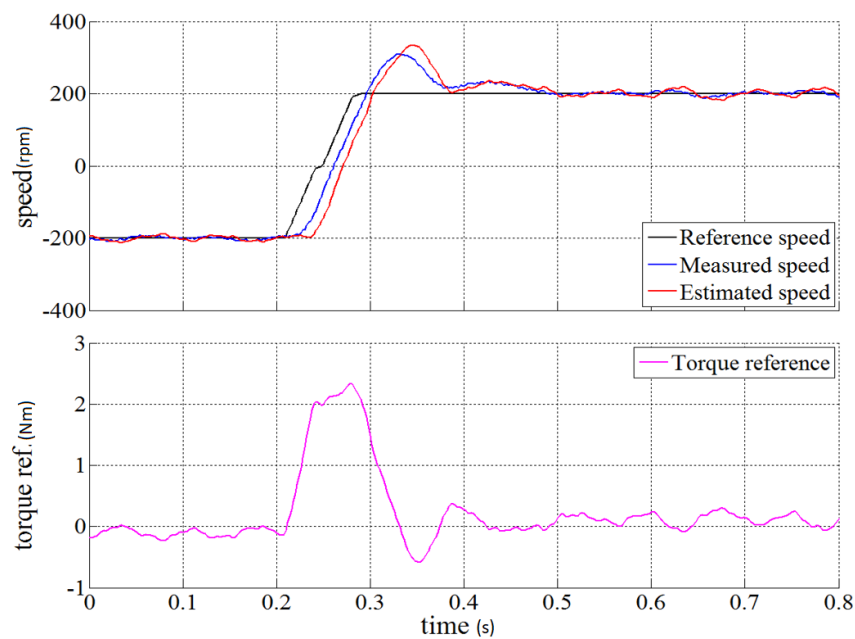


Figure 11. Motor #1: Sensorless speed control (MTPA), -200 to $+200$ rpm inversion, proposed (self-adaptation) rotating voltage injection, no load.

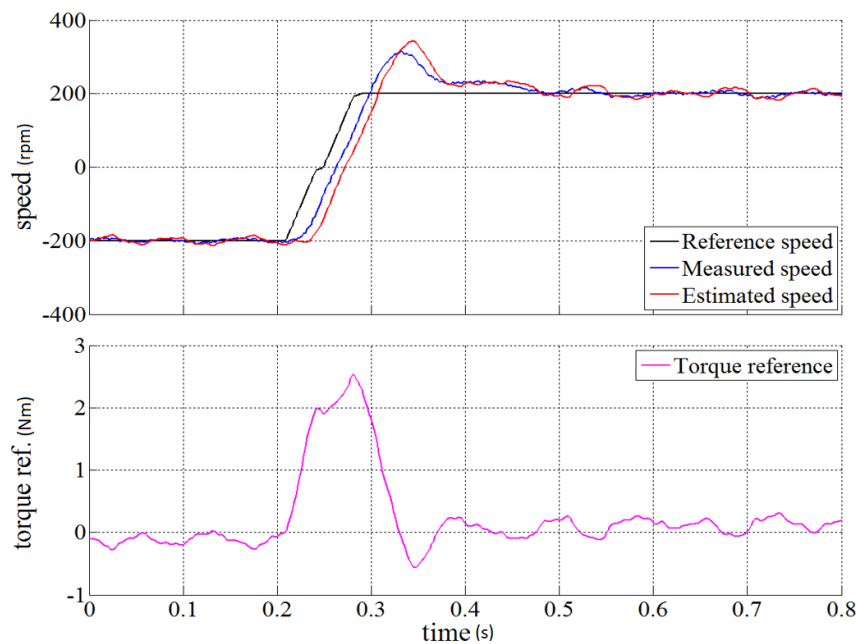


Figure 12. Motor #1: Sensorless speed control (MTPA), -200 to $+200$ rpm inversion, typical (no-adaptation) rotating voltage injection, no load.

Load disturbance rejection tests have also been carried out and reported in Figures 13 and 14. The brake is activated at 0.15 s, with a reference value of 6 Nm (90% nominal load), causing the speed to decrease and remain close to zero. In this condition, the speed regulator integral part increases almost linearly, until the brake torque is overcome. The speed oscillations in the loaded condition, around zero speed, are due to the passive nature of the brake, which suddenly increases the torque as the speed changes from zero, in fact a similar effect can be observed in simulation (Figure 8). The position estimation error remains acceptable during the whole experimental test. The results obtained using the proposed gain adaptation algorithm are very similar to those resulting from specific gain tuning (more accurate comparison will be provided at the end of this section), confirming that, thanks to the

proposed technique, the desired estimation dynamics can be achieved without using prior knowledge of the machine differential inductances.

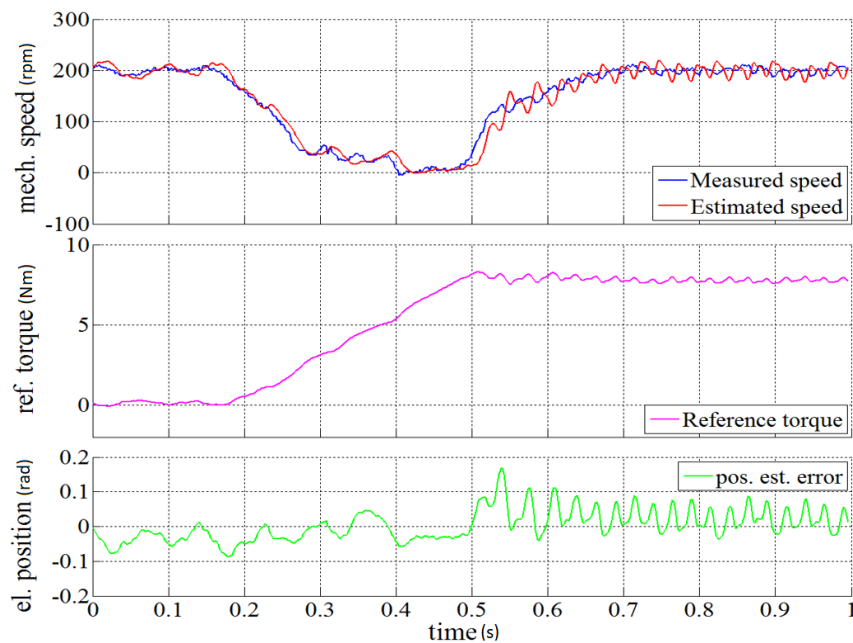


Figure 13. Motor #1: Sensorless speed control (MTPA), load disturbance at 200 rpm, 0 to 6 Nm load, proposed (self-adaptation) rotating voltage injection.

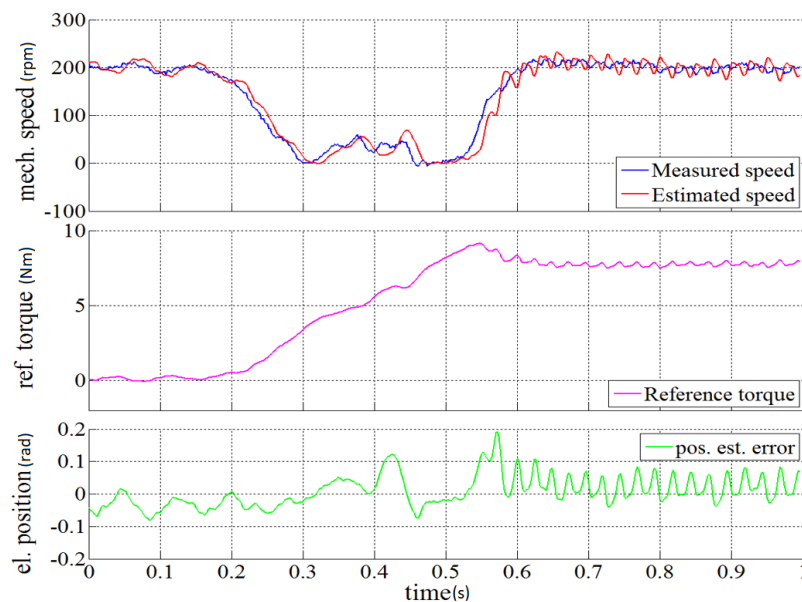


Figure 14. Motor #1: Sensorless speed control (MTPA), load disturbance at 200 rpm, 0 to 6 Nm load, typical (no-adaptation) rotating voltage injection.

The regulation capabilities of the i_{d1} and i_{q0} loops have also been tested for both machines, a selection of the obtained results will be shown hereafter. In Figure 15, while reference speed is kept constant at 200 rpm and the reference value for i_{d1} is set to 75 mA, torque load is increased in 1-Nm steps from 0 to 6 Nm. As has been done for the simulations reported in Figure 8, null d -axis current reference is imposed (i.e., MTPA is not applied) in order to stress the voltage adaptation mechanism. Due to the resulting heavy saturation on the q -axis, wide changes in the injected voltage magnitude (from about 30 to 60 V) are required in order to keep i_{d1} close to the reference value.

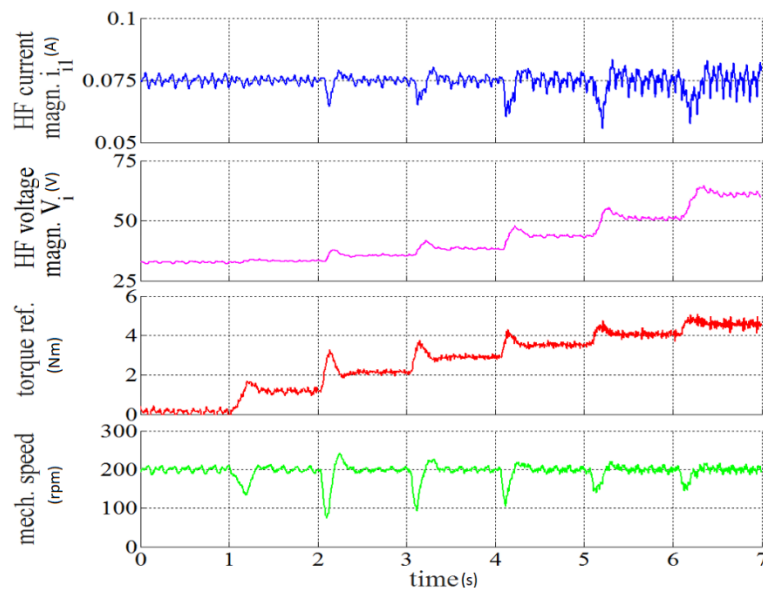


Figure 15. Motor #1: Sensorless speed control ($i_d^* = 0$), gain adaptation and i_{i1} regulation: 200 rpm, 1-Nm steps from 0 to 6 Nm.

Figure 16 demonstrates full sensorless control using both the proposed methods, i.e., PLL gain adaptation and high-frequency current regulation. A speed reversal command (-200 to $+200$ rpm) is followed by a sudden load increase and decrease, while gain adaptation is enabled and i_{i1} is regulated at 75 mA. Speed control performances are satisfactory and fulfil the control design specifications.

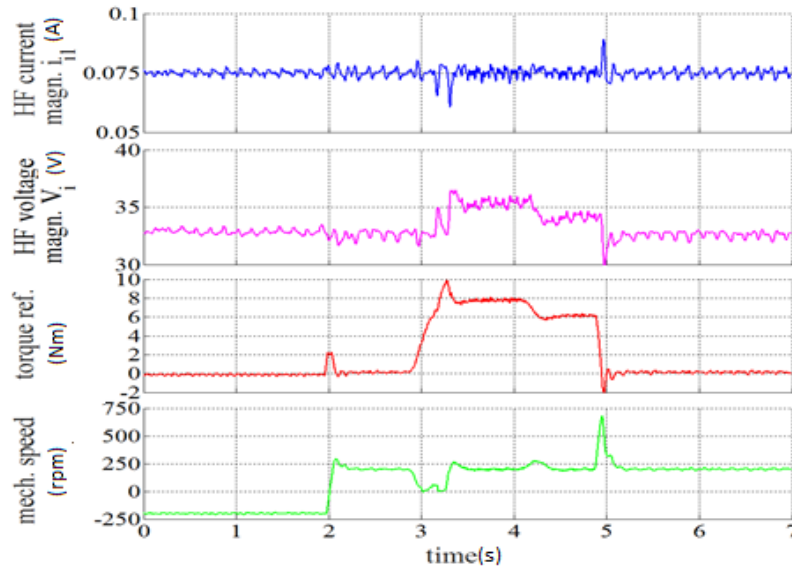


Figure 16. Motor #1: Sensorless speed control (MTPA), gain adaptation and i_{i1} regulation: -200 to $+200$ rpm, no-load to 6 Nm to no-load.

In Figure 17 motor #2 is considered. The same PLL parameters as for motor #1 (i.e., PLL gains and filters) have been adopted. Gain adaptation is enabled and regulation of i_{i0} is also active. Due to saturation, the injection voltage amplitude needs to be set in order to achieve $i_{i0} \approx 500$ mA. This value has been found to ensure robust operation of the sensorless control under full load disturbance. It is worth noticing that $i_{i0} = 500$ mA corresponds, at full-load, to i_{i1} being almost equal to 75 mA. This indirectly confirms that $i_{i1} \geq 75$ mA is approximately the minimal condition which ensures proper operation under full load, for the setup and dynamical response considered in experiments. This result

is independent of the method adopted, i.e., the same requirement applies to both the classical and the self-adaptation scheme. It is worth noticing that 75 mA is a very small amount of current with respect to the full-scale value of current sensing, since it corresponds to about 3 counts of the 12-bit ADC. If further investigations will confirm these findings, since the proposed automatic regulation is able to keep the “useful” HF current amplitude (I_{i1}) at an almost constant level under varying conditions, this could be a means for ensuring a certain signal-to-noise ratio of estimates and ultimately a certain robustness. Under these hypotheses, once the minimum level of HF current is determined (e.g., via experiments), the proposed HF current amplitude regulation could ensure injection of the minimum HF voltage required to satisfy the robustness requirements.

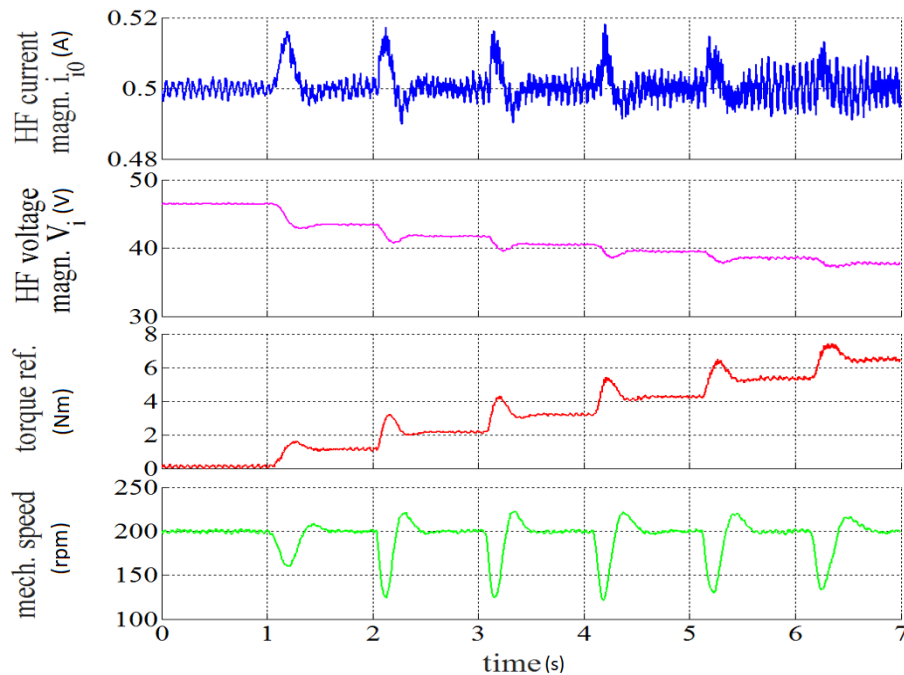


Figure 17. Motor#2: Sensorless speed control (MTPA), gain adaptation and i_{i0} regulation, 200 rpm, 1-Nm steps from 0 to 6 Nm.

The experimental tests demonstrate that, thanks to the proposed technique, motor magnetic parameters are not needed for the tuning of the PLL. Robust speed control is obtained, achieving dynamical performances and steady-state accuracy which perfectly match the reference method for rotating voltage injection [7], this being a hint of the correctness of the automatic adaptation of the tracking loop gain. Moreover, high-frequency current magnitude (i_{i1} or i_{i0}) can be regulated to a constant value, which leads to robust operation at different load levels applying small injection voltage.

Since different design choices for PLL gains and loop filter parameters will result in different dynamics, the estimation loop can be designed according to various bandwidth requirements. Generally, wider estimation bandwidth will allow to set the speed control for faster response, but will also result in larger estimation noise. As an example, an experiment has been carried out using increased PLL gains (twice the previously adopted values) and LPF bandwidth (double the value used in previous experiments), while the speed regulation proportional and integral gains were increased by 1.5 and 3 times, respectively. Figures 18 and 19 report the speed inversion (test conditions similar to Figures 11 and 12) and load torque disturbance tests (similar to Figures 13 and 14 respectively). In this case, the current reference values were generated according to the MTPA trajectory and gain adaptation was enabled, while i_{i1} was controlled to 0.15 A. As can be seen, after the sudden load increase in Figure 19, the speed decreases by approximately 100 rpm (about half the previous undershoot), while the response to quick speed reference change from -200 to 200 rpm (Figure 18) is slightly

faster (i.e., approximately 10 Hz bandwidth) with respect to Figures 11 and 12. Using these tuning rules, the steady-state speed ripple becomes much more relevant (especially on estimated speed) with respect to previous experiments, due to the wider bandwidth of the estimation loop and the faster speed loop reaction. The visible oscillations may be caused by a combination of different phenomena, such as current measurement noise or error and imperfect compensation of inverter voltage distortion. However, the main cause is probably the presence of anisotropy harmonics, also called “multiple saliencies”, [17]. A hint pointing to this effect is the dependency on the load, i.e., the fact that ripple increases with current magnitude, which may be due to the presence of local iron saturation. Compensating the error caused by these harmonics is possible, but requires a complex and time-consuming laboratory characterization, which is out of the scope of this work and in contrast with the application scenario intended for this proposal, i.e., industrial drives where little knowledge is available about the machine features.

The presence of a trade-off between estimation bandwidth and noise is a common feature in sensorless control, while determining the optimal choice is strongly related to the real application. It is also worth recalling that very low inertia as the load, as in this setup, is a worst-case condition for speed ripple.

Startup in two different conditions (no load and 6 Nm passive load) has also been tested for the two methods (proposed and typical). Gains have been tuned as in previous figures (“increased bandwidth”) and injection is performed by regulating the i_{i1} value to 150 mA with the proposed technique, while voltage magnitude is constant (70 V) for the non-adapted case. Also in these experiments, which results are reported in Figures 20–23, there is very good matching between the two methods.

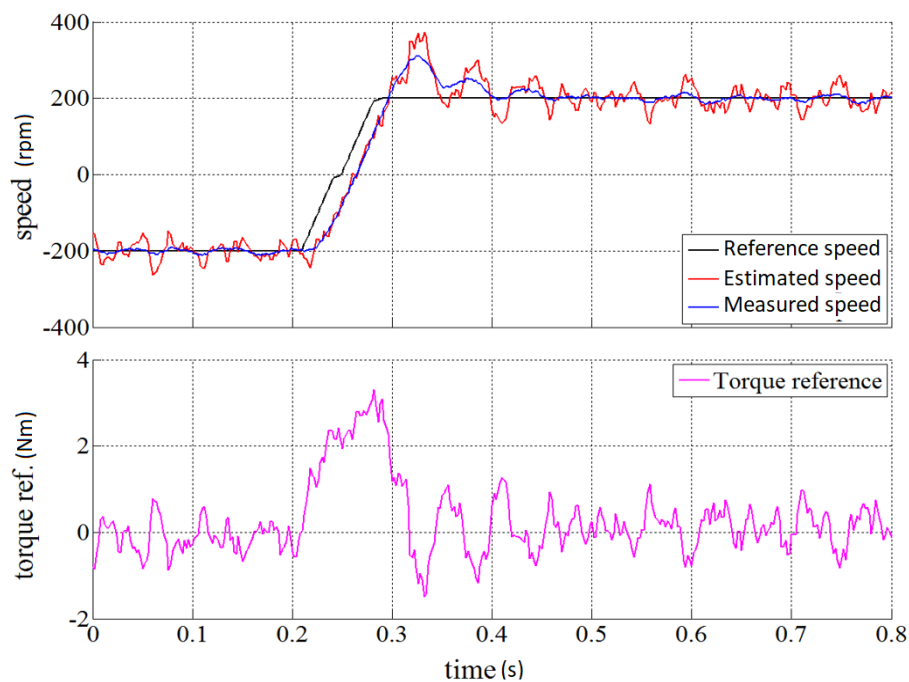


Figure 18. Motor #1: Increased bandwidth sensorless speed control (MTPA), -200 to $+200$ rpm inversion, proposed (self-adaptation) rotating voltage injection and i_{i1} regulation (150 mA), no load.

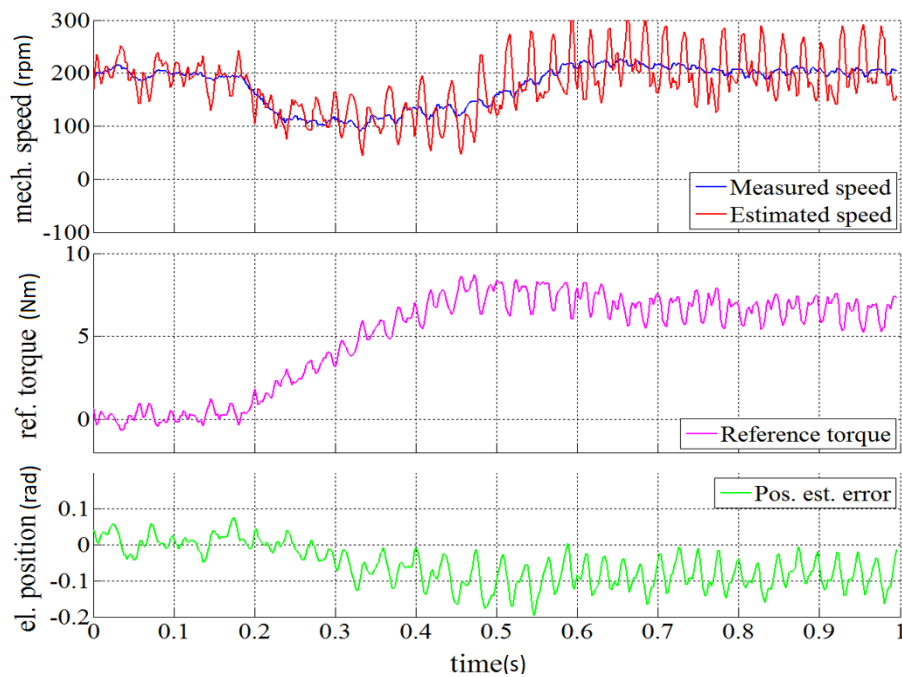


Figure 19. Motor #1: Increased bandwidth sensorless speed control (MTPA), load disturbance at 200 rpm, 0 to 6 Nm load, gain adaptation and i_{l1} regulation (150 mA).

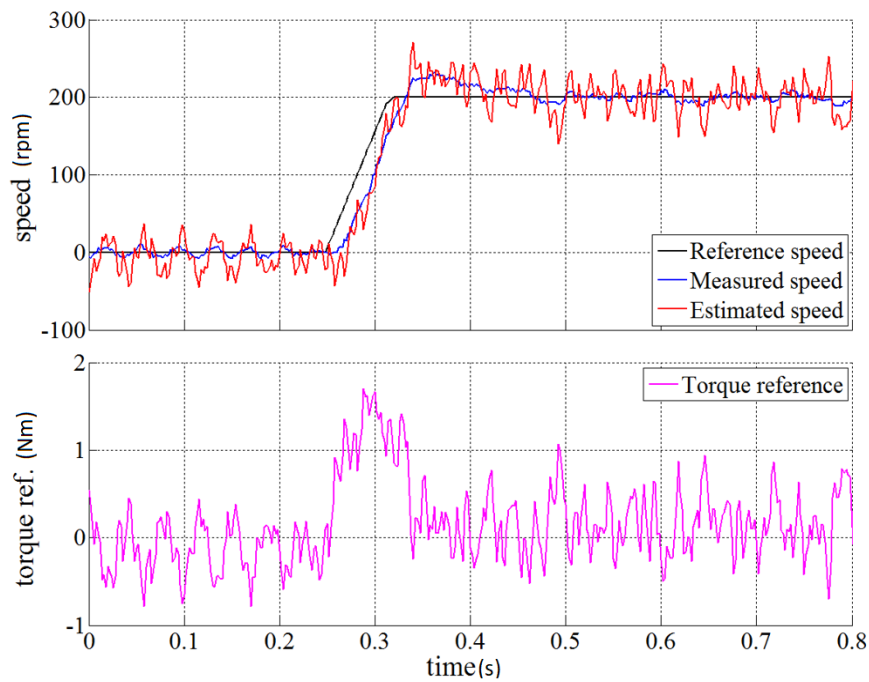


Figure 20. Motor #1: Increased bandwidth sensorless speed control (MTPA), startup from 0 to 200 rpm, proposed (self-adaptation) rotating voltage injection and i_{l1} regulation (150 mA), no load.

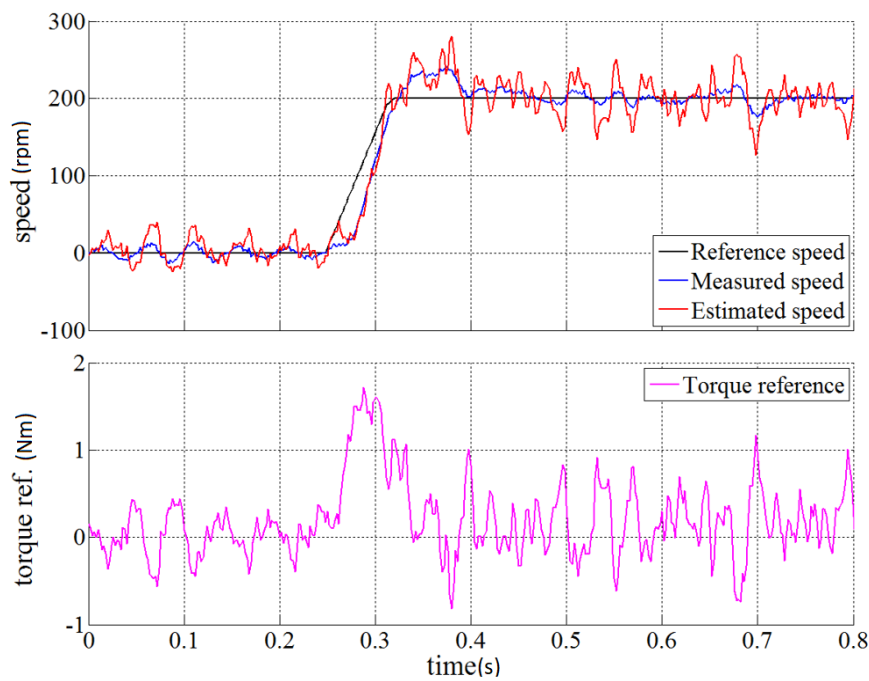


Figure 21. Motor #1: Increased bandwidth sensorless speed control (MTPA), startup from 0 to 200 rpm, typical (no adaptation) rotating voltage injection (70 V), no load.

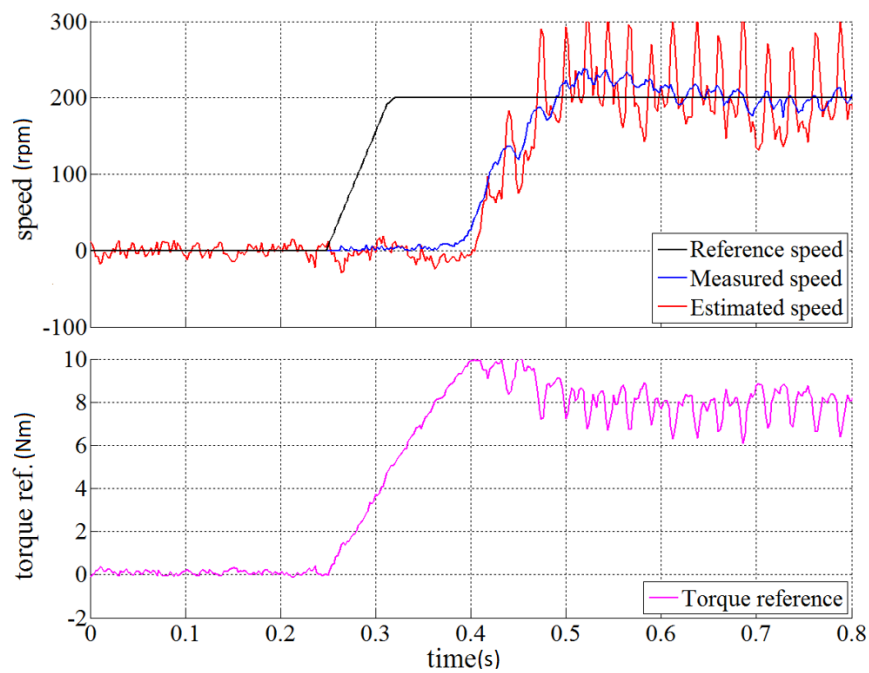


Figure 22. Motor #1: Increased bandwidth sensorless speed control (MTPA), startup from 0 to 200 rpm, proposed (self-adaptation) rotating voltage injection and i_{11} regulation (150 mA), 6 Nm load.

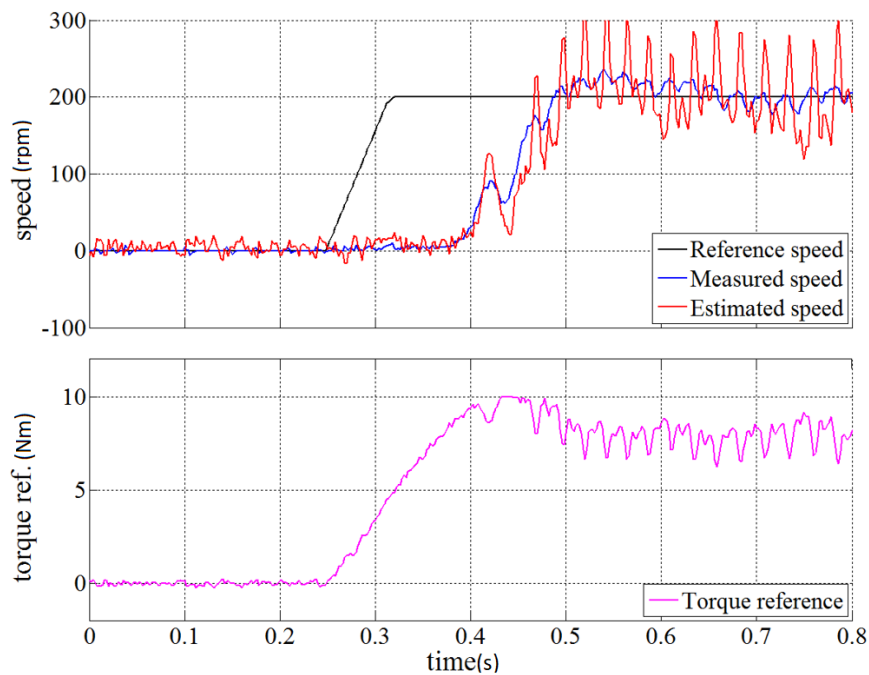


Figure 23. Motor #1: Increased bandwidth sensorless speed control (MTPA), startup from 0 to 200 rpm, typical (no adaptation) rotating voltage injection (70 V), 6 Nm load.

In order to better compare the performance of the proposed method with respect to the traditional one (i.e., no adaptation), a quantitative assessment has been carried out in terms of RMS error, calculated on different quantities, namely the speed estimation error, the speed control error and the position estimation error (when available in the acquisition). The corresponding data has been consolidated in Table 2. The data has been gathered for showing the equivalence of the two methods in terms of performance. Although the tests are too few to have any statistical significance, it can be seen that the various estimation and control errors are very close. This confirms that the aim of the paper has been reached, i.e., providing similar or better performance and robustness with respect to the traditional method, at the same time simplifying the tuning of the estimation algorithm (which does not require knowledge of motor characteristics) and ensuring consistent estimation dynamics with different machines and operating conditions.

Table 2. Quantitative comparison of error in experimental tests.

Test Type	Evaluation Type	Proposed	Traditional
Speed inversion, -200 to $+200$ rpm, no load (Figures 11 and 12)	RMS speed estimation error	19.2 rpm	18.9 rpm
	RMS speed control error	32.6 rpm	34.4 rpm
Disturbance rejection, 200 rpm, step load from 0 to 6 Nm (Figures 13 and 14)	RMS speed estimation error	15.5 rpm	17.1 rpm
	RMS speed control error	93.6 rpm	97.7 rpm
	RMS position estimation error	0.045 rad	0.049 rad
Startup, 0 to 200 rpm, no load (Figures 20 and 21)	RMS speed estimation error	19.6 rpm	19.2 rpm
	RMS speed control error	14.5 rpm	15.2 rpm
Startup, 0 to 200 rpm, 6 Nm load (Figures 22 and 23)	RMS speed estimation error	32.6 rpm	31.9 rpm
	RMS speed control error	69.1 rpm	70.6 rpm

8. Conclusions

An auto-tuning and self-adaptation method for a position and speed estimation algorithm based on rotating high-frequency voltage injection has been proposed in this paper, for application in sensorless IPMSM drives. Theoretical analysis, simulation, and experimental results demonstrate the possibility to specify the dynamical behavior of the position and speed estimation tracking loop, being invariant with respect to the rotor anisotropy level (i.e., different machine inductance values) and injected voltage magnitude. The proposed self-adaptation also allows the automatic tuning of the PLL gains with no a priori knowledge of the motor inductances, since the design procedure results in parameter values (gains and filters bandwidth) which lead to similar dynamics not only in different motor operating conditions, but also on different machines.

Moreover, the high-frequency current magnitude (either i_{i1} or i_{i0}) can be automatically regulated online, by varying the injected signal voltage amplitude in a closed-loop fashion. Experimental results suggest that this allows to minimize the HF current ripple, while preserving the robustness of the estimation process.

By applying the proposed technique, the tuning of estimation PLL is simplified and made independent of the machine characteristics. In fact, it is possible to adopt exactly the same algorithm, the same filters and PLL gains for different machines, obtaining the same position and speed tracking response. This has been demonstrated through theoretical analysis and specific experiments. The sensorless speed control has shown very similar or slightly improved performance with respect to the traditional method used as a benchmark, in terms of dynamical response and steady-state ripple (based on several experimental tests). No disadvantages have been observed in terms of performance, while the adoption of this method comes at the cost of a small increase in complexity and computational effort in the controller. On the other hand, from the point of view of developers and manufacturers, this seems to be generously compensated by great simplification of the tuning, higher reliability and robustness of the control, which would otherwise require fine tuning and/or complex compensation techniques, based on the detailed knowledge of motor parameters. The improvements brought by this proposal represent an important leap towards the automation of the tuning process in sensorless drives based on IPMSMs, which is expected to help developers in the adoption of advanced methods such as HF injection. Automatic tuning and self-adaptation, i.e., those procedures which relieve the final user from the effort of setting control parameters for proper operation of the drive, are considered of paramount importance for enabling a widespread use of this type of machines. Since interior PMSMs are potentially very efficient, compact and relatively low-cost (with respect to their surface mount counterparts), their wide utilization in industrial applications (which usually require sensorless operation due to cost and reliability reasons) is expected to bring important advantages.

Author Contributions: P.K. and S.C. developed the main idea of the paper, which has been discussed and analyzed by all the authors together. P.K. and S.C. carried out most of the work related to simulations and experimental investigation, with contributions by the other authors. The authors also worked together on the formal analysis, writing, editing and reviewing, under the supervision of L.A. and R.P.

Funding: This research received no external funding.

Acknowledgments: This work was supported by the Open Access Publishing Fund of the Free University of Bozen-Bolzano.

Conflicts of Interest: The authors declare no conflict of interest.

References

1. Bedetti, N.; Calligaro, S.; Petrella, R. Stand-Still Self-Identification of Flux Characteristics for Synchronous Reluctance Machines Using Novel Saturation Approximating Function and Multiple Linear Regression. *IEEE Trans. Ind. Appl.* **2016**, *52*, 3083–3092. [[CrossRef](#)]

2. Odhano, S.A.; Bojoi, R.; Roşu, Ş.G.; Tenconi, A. Identification of the Magnetic Model of Permanent-Magnet Synchronous Machines Using DC-Biased Low-Frequency AC Signal Injection. *IEEE Trans. Ind. Appl.* **2015**, *51*, 3208–3215. [[CrossRef](#)]
3. Odhano, S.A.; Giangrande, P.; Bojoi, R.I.; Gerada, C. Self-Commissioning of Interior Permanent-Magnet Synchronous Motor Drives with High-Frequency Current Injection. *IEEE Trans. Ind. Appl.* **2014**, *50*, 3295–3303. [[CrossRef](#)]
4. Bedetti, N.; Calligaro, S.; Petrella, R. Self-Commissioning of Inverter Dead-Time Compensation by Multiple Linear Regression Based on a Physical Model. *IEEE Trans. Ind. Appl.* **2015**, *51*, 3954–3964. [[CrossRef](#)]
5. Pescetto, P.; Pellegrino, G. Sensorless commissioning of synchronous reluctance machines augmented with high frequency voltage injection. In Proceedings of the 2017 IEEE Energy Conversion Congress and Exposition (ECCE), Cincinnati, OH, USA, 1–5 October 2017; pp. 1909–1916.
6. Schroedl, M. Sensorless control of AC Machines at Low Speed and Standstill based on the “INFORM”-method. In Proceedings of the IAS’96. Conference Record of the 1996 IEEE Industry Applications Conference Thirty-First IAS Annual Meeting, San Diego, CA, USA; 6–10 October 1996; pp. 270–277.
7. Jansen, P.L.; Lorenz, R.D. Transducerless position and velocity estimation in induction and salient AC machines. *IEEE Trans. Ind. Appl.* **1995**, *31*, 240–247. [[CrossRef](#)]
8. Consoli, A.; Russo, F.; Scarcella, G.; Testa, A. Low-and zero-Speed sensorless control of synchronous reluctance motors. *IEEE Trans. Ind. Appl.* **1999**, *35*, 1050–1057. [[CrossRef](#)]
9. Corley, M.J.; Lorenz, R.D. Rotor position and velocity estimation for a salient-Pole permanent magnet synchronous machine at standstill and high speeds. *IEEE Trans. Ind. Appl.* **1998**, *34*, 784–789. [[CrossRef](#)]
10. Bolognani, S.; Calligaro, S.; Petrella, R.; Tursini, M. Sensorless Control of IPM Motors in the Low-Speed Range and at Standstill by HF Injection and DFT Processing. *IEEE Trans. Ind. Appl.* **2011**, *47*, 96–104. [[CrossRef](#)]
11. Yoon, Y.D.; Sul, S.K.; Morimoto, S.; Ide, K. High bandwidth sensorless algorithm for AC machines based on square-wave type voltage injection. *IEEE Trans. Ind. Appl.* **2011**, *47*, 1361–1370. [[CrossRef](#)]
12. Paulus, D.; Landsmann, P.; Kennel, R. Sensorless field-Oriented control for permanent magnet synchronous machines with an arbitrary injection scheme and direct angle calculation. In Proceedings of the 2011 Symposium on Sensorless Control for Electrical Drives, Birmingham, UK, 1–2 September 2011.
13. Hua, Y.; Asher, G.M.; Sumner, M.; Gao, Q. Sensorless control of surface mounted permanent magnet machine using the standard space vector PWM. In Proceedings of the 2007 IEEE Industry Applications Annual Meeting, New Orleans, LA, USA, 23–27 September 2007; pp. 661–667.
14. Raute, R.; Caruana, C.; Cilia, J.; Staines, C.S.; Sumner, M. A zero speed operation sensorless PMSM drive without additional test signal injection. In Proceedings of the 2007 European Conference on Power Electronics and Applications, Aalborg, Denmark, 2–5 September 2007; pp. 1–10.
15. Guglielmi, P.; Pastorelli, M.; Vagati, A. Cross-Saturation Effects in IPM Motors and Related Impact on Sensorless Control. *IEEE Trans. Ind. Appl.* **2006**, *42*, 1516–1522. [[CrossRef](#)]
16. Seilmeier, M.; Piepenbreier, B. Sensorless Control of PMSM for the Whole Speed Range Using Two-Degree-of-Freedom Current Control and HF Test Current Injection for Low-Speed Range. *IEEE Trans. Power Electron.* **2015**, *30*, 4394–4403. [[CrossRef](#)]
17. Reigosa, D.D.; Garcia, P.; Raca, D.; Briz, F.; Lorenz, R.D. Measurement and Adaptive Decoupling of Cross-Saturation Effects and Secondary Saliencies in Sensorless Controlled IPM Synchronous Machines. *IEEE Trans. Ind. Appl.* **2008**, *44*, 1758–1767. [[CrossRef](#)]
18. Li, Y.; Zhu, Z.Q.; Howe, D.; Bingham, C.M.; Stone, D. Improved Rotor Position Estimation by Signal Injection in Brushless AC Motors, Accounting for Cross-Coupling Magnetic Saturation. In Proceedings of the 2007 IEEE Industry Applications Annual Meeting, New Orleans, LA, USA, 23–27 September 2007; pp. 2357–2364.
19. Kim, S.Y.; Ha, I.J. A New Observer Design Method for HF Signal Injection Sensorless Control of IPMSMs. *IEEE Trans. Ind. Electron.* **2008**, *55*, 2525–2529.
20. Cupertino, F.; Giangrande, P.; Salvatore, L.; Pellegrino, G. Model based design of a sensorless control scheme for permanent magnet motors using signal injection. In Proceedings of the 2010 IEEE Energy Conversion Congress and Exposition, Atlanta, GA, USA, 12–16 September 2010; pp. 3139–3146.
21. Piippo, A.; Hinkkanen, M.; Luomi, J. Analysis of an Adaptive Observer for Sensorless Control of Interior Permanent Magnet Synchronous Motors. *IEEE Trans. Ind. Electron.* **2008**, *55*, 570–576. [[CrossRef](#)]

22. Seilmeier, M.; Ebersberger, S.; Piepenbreier, B. HF Test Current Injection-Based Self-Sensing Control of PMSM for Low-and Zero-Speed Range Using Two-Degree-of-Freedom Current Control. *IEEE Trans. Ind. Appl.* **2015**, *51*, 2268–2278. [[CrossRef](#)]
23. Xie, G.; Lu, K.; Dwivedi, S.K.; Rosholm, J.R.; Blaabjerg, F. Minimum-Voltage Vector Injection Method for Sensorless Control of PMSM for Low-Speed Operations. *IEEE Trans. Power Electron.* **2016**, *31*, 1785–1794. [[CrossRef](#)]
24. Alberti, L.; Bottesi, O.; Calligaro, S.; Kumar, P.; Petrella, R. Self-Adaptive high-Frequency injection based sensorless control for IPMSM and SynRM. In Proceedings of the 2017 IEEE International Symposium on Sensorless Control for Electrical Drives (SLED), Catania, Italy, 18–19 September 2017; pp. 97–102.
25. Bugsch, M.; Piepenbreier, B. HF Test Current-Ripple-Control-Based Sensorless Method for SynRMs in the Low-and Zero-Speed Range Leading to an Adaptive Square-Wave-Shaped Voltage Injection. In Proceedings of the 2018 IEEE 9th International Symposium on Sensorless Control. for Electrical Drives (SLED), Helsinki, Finland, 13–14 September 2018; pp. 24–29.
26. Park, R.H. Two-Reaction theory of synchronous machines generalized method of analysis-Part I. *Trans. Am. Inst. Electr. Eng.* **1929**, *48*, 716–727. [[CrossRef](#)]
27. ABB Industrial Drives ACS880 Primary Control Programming Firmware Manual, ABB Pvt. Ltd. Available online: <https://www.search-ext.abb.com/library/Download.aspx?DocumentID=3AUA0000085967&LanguageCode=en&DocumentPartId=1&Action=Launch> (accessed on 23 September 2019).
28. COMBIVERT F6 Programming Manual, KEB Automation KG, 2017. Available online: http://www.keb.de/fileadmin/media/Manuals/dr/ma_dr_f6-cu-ak-22-phb-20142926_en.pdf (accessed on 23 September 2019).
29. COMBIVERT F5 Application Manual, KEB Automation KG, 2015. Available online: <https://www.keb.it/fileadmin/media/Manuals/f5/control/f5a/00f5aeak450.pdf> (accessed on 23 September 2019).
30. Luo, X.; Tang, Q.; Shen, A.; Zhang, Q. PMSM Sensorless Control by Injecting HF Pulsating Carrier Signal into Estimated Fixed-Frequency Rotating Reference Frame. *IEEE Trans. Ind. Electron.* **2016**, *63*, 2294–2303. [[CrossRef](#)]
31. Yu, S.; Zhang, W.; Yao, S. Rotating high-Frequency voltage injection based on characteristic harmonic elimination. In Proceedings of the 2016 19th International Conference on Electrical Machines and Systems (ICEMS), Chiba, Japan, 13–16 November 2016; pp. 1–5.
32. Alaei, A.; Lee, D.; Ahn, J.; Nejad, S.M.S. Dynamic performance analysis of high frequency signal injection based sensorless methods for IPM synchronous motors. In Proceedings of the 2018 9th Annual Power Electronics, Drives Systems and Technologies Conference (PEDSTC), Tehran, Iran, 13–15 February 2018; pp. 151–156.
33. Mizutani, R.; Takeshita, T.; Matsui, N. Current model-based sensorless drives of salient-pole PMSM at low speed and standstill. *IEEE Trans. Ind. Appl.* **1998**, *34*, 841–846. [[CrossRef](#)]
34. Raca, D.; Garcia, P.; Reigosa, D.D.; Briz, F.; Lorenz, R.D. Carrier-Signal Selection for Sensorless Control of PM Synchronous Machines at Zero and Very Low Speeds. *IEEE Trans. Ind. Appl.* **2010**, *46*, 167–178. [[CrossRef](#)]
35. Choi, C.; Seok, J. Pulsating Signal Injection-Based Sensorless Control of PMSM Using Injection Axis Switching Scheme without Additional Offline Commissioning Test. In Proceedings of the 2007 IEEE Industry Applications Annual Meeting, New Orleans, LA, USA, 23–27 September 2007; pp. 2365–2370.
36. Kim, H.; Lorenz, R.D. Carrier signal injection based sensorless control methods for IPM synchronous machine drives. In Proceedings of the Conference Record of the 2004 IEEE Industry Applications Conference, 2004. 39th IAS Annual Meeting, Seattle, WA, USA, 3–7 October 2004; pp. 977–984.
37. Liu, J.M.; Zhu, Z.Q. Novel Sensorless Control Strategy with Injection of High-Frequency Pulsating Carrier Signal Into Stationary Reference Frame. *IEEE Trans. Ind. Appl.* **2014**, *50*, 2574–2583. [[CrossRef](#)]
38. Lin, T.C.; Zhu, Z.Q. Sensorless Operation Capability of Surface-Mounted Permanent-Magnet Machine Based on High-Frequency Signal Injection Methods. *IEEE Trans. Ind. Appl.* **2015**, *51*, 2161–2171. [[CrossRef](#)]
39. Zhu, Z.Q.; Gong, L.M. Investigation of Effectiveness of Sensorless Operation in Carrier-Signal-Injection-Based Sensorless-Control Methods. *IEEE Trans. Ind. Electron.* **2011**, *58*, 3431–3439. [[CrossRef](#)]
40. Kim, D.; Kwon, Y.; Sul, S.; Kim, J.; Yu, R. Suppression of Injection Voltage Disturbance for High-Frequency Square-Wave Injection Sensorless Drive with Regulation of Induced High-Frequency Current Ripple. *IEEE Trans. Ind. Appl.* **2016**, *52*, 302–312. [[CrossRef](#)]
41. Wang, G.; Liu, R.; Zhao, N.; Ding, D.; Xu, D. Enhanced Linear ADRC Strategy for HF Pulse Voltage Signal Injection-Based Sensorless IPMSM Drives. *IEEE Trans. Power Electron.* **2019**, *34*, 514–525. [[CrossRef](#)]

42. Roetzer, M.; Vollmer, U.; Kennel, R.M. Demodulation Approach for Slowly Sampled Sensorless Field-Oriented Control Systems Enabling Multiple-Frequency Injections. *IEEE Trans. Ind. Appl.* **2018**, *54*, 732–744. [[CrossRef](#)]
43. Wang, G.; Yang, L.; Zhang, G.; Zhang, X.; Xu, D. Comparative Investigation of Pseudorandom High-Frequency Signal Injection Schemes for Sensorless IPMSM Drives. *IEEE Trans. Power Electron.* **2017**, *32*, 2123–2132. [[CrossRef](#)]
44. Jung, S.; Ha, J. Analog Filtering Method for Sensorless AC Machine Control with Carrier-Frequency Signal Injection. *IEEE Trans. Ind. Electron.* **2015**, *62*, 5348–5358. [[CrossRef](#)]
45. Vaez-Zadeh, S. *Control of Permanent Magnet Synchronous Motors*; Oxford University Press: Oxford, UK, 2018.
46. Andreescu, G.; Pitic, C.I.; Blaabjerg, F.; Boldea, I. Combined Flux Observer with Signal Injection Enhancement for Wide Speed Range Sensorless Direct Torque Control of IPMSM Drives. *IEEE Trans. Energy Conv.* **2008**, *23*, 393–402. [[CrossRef](#)]
47. Silva, C.; Asher, G.M.; Sumner, M. Hybrid rotor position observer for wide speed-Range sensorless PM motor drives including zero speed. *IEEE Trans. Ind. Electron.* **2006**, *53*, 373–378. [[CrossRef](#)]
48. Guglielmi, P.; Pastorelli, M.; Vagati, A. Impact of cross-Saturation in sensorless control of transverse-Laminated synchronous reluctance motors. *IEEE Trans. Ind. Electron.* **2006**, *53*, 429–439. [[CrossRef](#)]
49. Hammel, W.; Kennel, R.M. Position sensorless control of PMSM by synchronous injection and demodulation of alternating carrier voltage. In Proceedings of the 2010 First Symposium on Sensorless Control for Electrical Drives, Padova, Italy, 9–10 July 2010; pp. 56–63.
50. Piippo, A.; Hinkkanen, M.; Luomi, J. Sensorless control of PMSM drives using a combination of voltage model and HF signal injection. In Proceedings of the Conference Record of the 2004 IEEE Industry Applications Conference, 2004. 39th IAS Annual Meeting, Seattle, WA, USA, 3–7 October 2004; Volume 2, pp. 964–970.
51. Wallmark, O.; Harnfors, L.; Carlson, O. An improved speed and position estimator for salient permanent-magnet synchronous motors. *IEEE Trans. Ind. Electron.* **2005**, *52*, 255–262. [[CrossRef](#)]
52. Yang, S.; Hsu, Y. Full Speed Region Sensorless Drive of Permanent-Magnet Machine Combining Saliency-Based and Back-EMF-Based Drive. *IEEE Trans. Ind. Electron.* **2017**, *64*, 1092–1101. [[CrossRef](#)]
53. Li, Y.; Taylor, A.; Bai, K. A hybrid observer for the full-Speed-Range sensorless control of interior permanent magnet motor drives. In Proceedings of the 2014 IEEE Transportation Electrification Conference and Expo (ITEC), Dearborn, MI, USA, 15–18 June 2014; pp. 1–5.
54. Bolognani, S.; Faggion, A.; Fornasiero, E.; Sgarbossa, L. Full speed range sensorless IPM motor drives. In Proceedings of the 2012 XXth International Conference on Electrical Machines, Marseille, France, 2–5 September 2012; pp. 2209–2215.



© 2019 by the authors. Licensee MDPI, Basel, Switzerland. This article is an open access article distributed under the terms and conditions of the Creative Commons Attribution (CC BY) license (<http://creativecommons.org/licenses/by/4.0/>).